



Hydrochemical interactions of phoretic particles: a regularized multipole framework

Francisco Rojas-Pérez^{1,2}, Blaise Delmotte¹ and Sébastien Michelin^{1,†}

¹LadHyX, CNRS, Ecole Polytechnique, Institut Polytechnique de Paris, 91120 Palaiseau, France

²Escuela de Física, Instituto Tecnológico de Costa Rica, Cartago, 159-7050, Costa Rica

(Received 22 December 2020; revised 23 April 2021; accepted 26 April 2021)

Chemically active colloids modify the concentration of chemical solutes surrounding them in order to self-propel. In doing so, they generate long-ranged hydrodynamic flows and chemical gradients that modify the trajectories of other particles. As a result, the dynamics of reactive suspensions is fundamentally governed by hydro-chemical interactions. A full solution of the detailed hydro-chemical problem with many particles is challenging and computationally expensive. Most current methods rely on the Green's functions of the Laplace and Stokes operators to approximate the particle signatures in the far field, an approach which is only valid in the very dilute limit in simple geometries. To overcome these limitations, we propose a regularized multipole framework, directly inspired by the force coupling method (FCM), to model phoretic suspensions. Our approach, called diffusio-phoretic FCM (DFCM), relies on grid-based volume averages of the concentration field to compute the particle surface concentration moments. These moments define the chemical multipoles of the diffusion (Laplace) problem and provide the swimming forcing of the Stokes equations. Unlike far-field models based on singularity superposition, DFCM accounts for mutually induced dipoles. The accuracy of the method is evaluated against exact and accurate numerical solutions for a few canonical cases. We also quantify its improvements over far-field approximations for a wide range of inter-particle distances. The resulting framework can readily be implemented into efficient solvers, allowing for large scale simulations of semi-dilute diffusio-phoretic suspensions.

Key words: active matter, micro-organism dynamics

1. Introduction

Many microscopic organisms and colloidal particles swim by exerting active stresses on the surrounding fluid in order to overcome its viscous resistance. In doing so, they

† Email address for correspondence: sebastien.michelin@ladhyx.polytechnique.fr

set their fluid environment into motion and modify the dynamics of their neighbours (Lauga & Powers 2009; Elgeti, Winkler & Gompper 2015). Large scale collective behaviour can emerge from the resulting long-ranged interactions between individual agents (Pedley & Kessler 1992; Zöttl & Stark 2016), but also profound modifications of the effective macroscopic rheological and transport properties of such active suspensions (Saintillan & Shelley 2013; Saintillan 2018). These have recently become a major focus to study a broader class of systems that are fundamentally out of thermodynamic equilibrium, broadly referred to as active matter systems, which comprise large assemblies of individually active agents that convert locally stored energy into mechanical actuation resulting in non-trivial effective macroscopic properties (Marchetti *et al.* 2013; Bechinger *et al.* 2016).

Most biological swimmers apply such active stresses to the fluid through sequences of shape changes, or swimming strokes, commonly through the flapping of slender flexible appendages such as flagella or cilia (Brennen & Winet 1977; Lauga & Powers 2009; Lauga 2016). Such cell motility in viscous fluids plays a critical role in a diversity of biological processes including mammal fertility (Fauci & Dillon 2006) and the balance of marine life ecosystems (Guasto, Rusconi & Stocker 2012). Inspired by these biological examples and many promising applications in various fields such as biomedicine or biochemical reactors, researchers and engineers across disciplines have focused on the design of microscopic self-propelled systems (Ebbens & Howse 2010). Many earlier designs were directly inspired by the rotation of the helical flagella of bacteria or the flapping of flexible cilia (Dreyfus *et al.* 2005; Zhang *et al.* 2009; Babataheri *et al.* 2011), but rely on complex miniaturization processes of moving parts or a macroscopic actuation (e.g. magnetic fields).

A fundamentally different route, explored more recently, exploits interfacial processes to generate fluid flow from local physico-chemical gradients (e.g. temperature, chemical potential, electric potential or solute concentration), resulting directly from a chemical activity of the particle surface itself (e.g. catalytic reactions) (Yadav *et al.* 2015; Moran & Posner 2017). The most famous and commonly used design is that of Janus nano- or micro-particles with two different catalytic or physical properties (Paxton *et al.* 2004; Perro *et al.* 2005). In dilute suspensions, these colloids exhibit short-term ballistic behaviour (with velocities reaching a few $\mu\text{m s}^{-1}$) but their long-time dynamics is more diffusive as the result of thermal fluctuations (Howse *et al.* 2007). In contrast, complex collective behaviour is observed in denser suspensions with the coexistence of cluster and gas-like phases (Theurkauff *et al.* 2012; Ginot *et al.* 2018). Understanding the emergence of such phase separation is currently a leading challenge in active matter physics (Cates & Tailleur 2015). Beyond their fundamental interest and the puzzling details of their individual and collective self-propulsions, these active colloids are already considered for various engineering or biomedical applications, including drug delivery (Kagan *et al.* 2010), micro-surgery (Shao *et al.* 2018), intelligent cargo delivery (Sundararajan *et al.* 2008), self-healing microchips (Li *et al.* 2015), chemical analysis (Duan *et al.* 2015) and sensing (Yi *et al.* 2016).

To generate autonomous propulsion, chemically active colloids exploit a combination of two different physico-chemical properties (Golestanian, Liverpool & Ajdari 2007; Moran & Posner 2017). The first one is a phoretic mobility, namely the ability to generate slip flow along the boundary of a colloidal particle in response to gradients of a solute (diffusio-phoresis), temperature (thermophoresis) or electric potential (electrophoresis) (Anderson 1989), resulting in a net drift of this particle. The second one is the ability of the particle itself to generate the local gradients through a surface activity, e.g.

surface catalysis of chemical reactions (Wang *et al.* 2006) or heat release (Bregulla & Cichos 2015). The combination of these two generic properties, or self-phoresis, provides the colloid with the ability to swim (Golestanian *et al.* 2007). Other self-propulsion mechanisms also share important similarities with self-phoresis, including the propulsion of active droplets (Maass *et al.* 2016) or of light-illuminated colloids in binary mixtures (Buttinoni *et al.* 2012). For simplicity, we focus on self-diffusio-phoresis of particles absorbing or releasing neutral chemical solutes (Córdova-Figueroa & Brady 2008; Popescu, Uspal & Dietrich 2016), keeping in mind that the approach and framework presented here can be applied or generalized to account for more generic self-phoretic systems (Moran & Posner 2011; Yariv 2011; Ibrahim, Golestanian & Liverpool 2017).

Symmetry breaking is an intrinsic requirement for directed motion in viscous flows; for self-phoretic colloids, this requires the colloid to create or sustain a chemical surface polarity. As a result, strictly isotropic colloids cannot self-propel individually, although they may do so by self-assembling into geometrically or chemically asymmetric structures (Soto & Golestanian 2014, 2015; Varma, Montenegro-Johnson & Michelin 2018; Schmidt *et al.* 2019). In practice, most chemically active colloids thus exhibit an intrinsic chemical asymmetry, where the two sides of a Janus colloid capture or release solutes of different natures or at different rates (Moran & Posner 2017). Geometrically asymmetric colloids also break the symmetry of their chemical environment and may thus self-propel (Kümmel *et al.* 2013; Shklyae, Brady & Córdova-Figueroa 2014; Michelin & Lauga 2015). A third route to symmetry breaking, based on an instability, arises for isotropic colloids when the chemical solutes diffuse sufficiently slowly for the nonlinear convective coupling of phoretic flows and chemical transport to become significant (Michelin, Lauga & Bartolo 2013; Izri *et al.* 2014; Hu *et al.* 2019).

Like all microswimmers, Janus phoretic particles self-propel by stirring the fluid around them, thus modifying the trajectory and speed of their neighbours. Due to their chemical activity, they also alter their chemical environment and thus also drive an additional phoretic motion of the surrounding particles. In most experiments on chemically active particles, the diffusing solutes are small (e.g. dissolved gas) and chemical transport is dominated by diffusion. Such micron-size colloids typically propel with velocities $U \approx 1\text{--}10 \mu\text{m s}^{-1}$ and consume or release solutes of diffusivity $D \approx 10^3 \mu\text{m}^2 \text{s}^{-1}$, so that the relevant Péclet number Pe is always small ($Pe \approx 10^{-3}\text{--}10^{-2}$) (Paxton *et al.* 2004; Howse *et al.* 2007; Theurkauff *et al.* 2012; Brown & Poon 2014). Obtaining the swimming velocity of phoretic Janus particles therefore requires the solution of two different problems sequentially, namely (i) a diffusion (Laplace) problem for the solute concentration around the colloids and (ii) a hydrodynamic (Stokes) problem for the fluid flow around them. Analytical solution is in general amenable only for single particles (Golestanian *et al.* 2007), although determining the coupled motion of two Janus colloids is also possible semi-analytically (Sharifi-Mood, Mozzafari & Córdova-Figueroa 2016; Varma & Michelin 2019; Nasouri & Golestanian 2020a). For more than two particles, a complete description of the phoretic motion requires numerical treatment (Montenegro-Johnson, Michelin & Lauga 2015) but with a computational cost that increases rapidly with the number of particles, motivating the use of reduced models for the particles' interactions.

In dilute suspensions, i.e. when particles are far apart from each other, their hydro-chemical interactions can be accounted for through the slowest-decaying chemical and hydrodynamic signatures of individual particles and their effect on their neighbours (Saha, Golestanian & Ramaswamy 2014; Varma & Michelin 2019). Due to their simplicity, small computational cost for a large number of particles and ability to handle the effect

of confinements through image systems, far-field models have been extensively used to analyse the motion of active suspensions (see e.g. Ibrahim & Liverpool 2016; Thutupalli *et al.* 2018; Kanso & Michelin 2019; Liebchen & Löwen 2019). An alternative mean-field approach describes the particles' motion in the ambient chemical and hydrodynamic fields generated by the superposition of their individual far-field signatures (Liebchen *et al.* 2015; Traverso & Michelin 2020).

For more concentrated suspensions, i.e. when the inter-particle distance is reduced, far-field models are not accurate as finite-size effects of the particles are no longer negligible. Although it is possible to include higher-order corrections using the method of reflections (Varma & Michelin 2019), more complex numerical models are in general required to solve the dual hydro-chemical problem accurately within not-so-dilute suspensions. Due to the mathematical similarities between the Laplace and Stokes problems, it is possible to draw inspiration from and build upon a large variety of methods already used in recent years for the numerical modelling of passive and active suspensions. A popular example is the Stokesian dynamics and its more recent extensions (Brady & Bossis 1988; Sierou & Brady 2001; Swan, Brady & Moore 2011; Fiore & Swan 2019), from which an analogous approach was proposed to solve for diffusion problems (Yan & Brady 2016). A similar approach relies on a truncated spectral expansion of the integral formulation of the Laplace and Stokes equations with tensorial spherical harmonics on the particle's surface (Singh & Adhikari 2019; Singh, Adhikari & Cates 2019). But the possible routes also include boundary element methods (Ishikawa, Simmonds & Pedley 2006; Montenegro-Johnson *et al.* 2015; Uspal *et al.* 2015), immersed boundary methods (Bhalla *et al.* 2013; Lambert *et al.* 2013; Lushi & Peskin 2013), lattice-Boltzmann approaches (Ladd & Verberg 2001; Alarcón & Pagonabarraga 2013), multi-particle collision dynamics (Yang, Wysocki & Ripoll 2014; Zöttl & Stark 2014; Colberg & Kapral 2017; Zöttl & Stark 2018) and the force coupling method (Maxey & Patel 2001; Delmotte *et al.* 2015).

The objective of the present work is to extend the fundamental idea and framework of the latter to establish and validate a unified method that accounts for both chemical and hydrodynamic interactions between phoretic particles. The force coupling method (FCM), used to solve for the hydrodynamic interactions of particles in a fluid, relies on the classical multipolar expansion of the solution for Stokes' equation (Saffman 1973), but proposes a regularized alternative to the singular Green's function in the form of smoothed Gaussian kernels. Beyond the obvious numerical advantage of such a regularization, it also provides an indirect route to account for the finite size of the particles through the finite support of these kernels. The FCM framework was initially proposed twenty years ago by Maxey and coworkers (Maxey & Patel 2001; Lomholt & Maxey 2003) to analyse the joint dynamics of passive spherical particles sedimenting in a viscous fluid. It has since then been extended to account for finite inertia (Xu, Maxey & Karniadakis 2002), lubrication effects (Dance & Maxey 2003) and non-sphericity of the particles (Liu *et al.* 2009), leading to a powerful method to study the hydrodynamic interactions of large suspensions. More recently, FCM was also adapted to account for the activity of the colloids and enabled the analysis of microswimmer suspensions (Delmotte *et al.* 2015).

In this work, an FCM-based method is presented to solve the Laplace problem for the concentration field in phoretic suspensions of spherical Janus particles, using a regularized multipole representation of the concentration based on smoothed kernels instead of the classical singular monopole and dipole singularities. This provides the phoretic forcing introduced by the local inhomogeneity of the concentration field on each particle, from which the hydrodynamic problem can be solved using the existing FCM approach for

active suspensions (Delmotte *et al.* 2015). Taken together, this provides an integrated framework to solve for the complete diffusio-phoretic problem, or diffusio-phoretic FCM, whose fundamental justification and validation is the main objective of the present work.

The rest of the paper is organized as follows. The governing equations for the collective motion of phoretic particles are first recalled in § 2. The diffusio-phoretic FCM (DFCM) is then presented in detail in § 3. More specifically, the new solution framework for the Laplace problem is first presented in § 3.1. Section 3.2 summarizes the main elements of the classical hydrodynamic FCM method and its extension to active particles, and § 3.3 finally presents how the two steps are conveniently coupled to solve successively the chemical and hydrodynamic problems. In order to validate the approach and compare its accuracy to existing methods, § 4 considers a series of canonical configurations for pairwise interactions of two Janus particles, for which an analytical or numerical solution of the full problem is available for any inter-particle distance. The results of DFCM are compared to this benchmark but also to the far-field estimation of the particles' velocities. This provides further insight into the improvement brought by this approach and its range of validity, which will be critical information for future use in larger suspension simulations. Finally, § 5 summarizes the findings of the paper, the constraints and advantages of the method and discusses some perspectives for its future implementation in studying large phoretic suspensions.

2. Modelling reactive suspensions

Reactive suspensions consist of large sets of micro-particles that are able to self-propel in a viscous fluid by exploiting the chemical activity of their surface and its ability to generate an effective hydrodynamic slip in response to gradients of the solute species they produce or consume. As a result, these particles react to the chemical and hydrodynamic forcing exerted by their neighbours, introducing a coupling that may lead to modified effective properties at the scale of the suspensions. For purely diffusive solute species, determining their individual dynamics requires solving successively for two different problems, namely a Laplace problem for the solute concentration distribution, followed by a Stokes problem for the hydrodynamic fields and particle velocities (translation and rotation) in response to the solute gradients at their surface (Golestanian *et al.* 2007). The corresponding equations of motion are recalled in detail below.

2.1. Governing equations for self-diffusio-phoresis of N micro-particles

The coupled motion of N identical and spherical phoretic particles of equal radius a is considered within a viscous fluid of density ρ and viscosity μ . Particle n occupies a volume V_n bounded by its surface S_n and centred at $Y_n(t)$, and has orientation \mathbf{p}_n ; U_n and $\mathbf{\Omega}_n$ are its translation and rotation velocities. The fluid domain is denoted V_f and may be bounded or unbounded (figure 1a).

Each particle emits a chemical solute of diffusivity D on the catalytic parts of its surface with a fixed spatially dependent rate, of characteristic magnitude α_0 , and is able to generate a slip flow in response to a surface concentration gradient, with a characteristic phoretic mobility M_0 . In the following, all variables and equations are made dimensionless using a , $U_0 = \alpha_0 M_0 / D$ and $a\alpha_0 / D$ as characteristic length, velocity and concentration scales.

As a result of its surface activity, the dimensionless relative concentration c (with respect to its background value far from the particles) satisfies the following Neumann condition

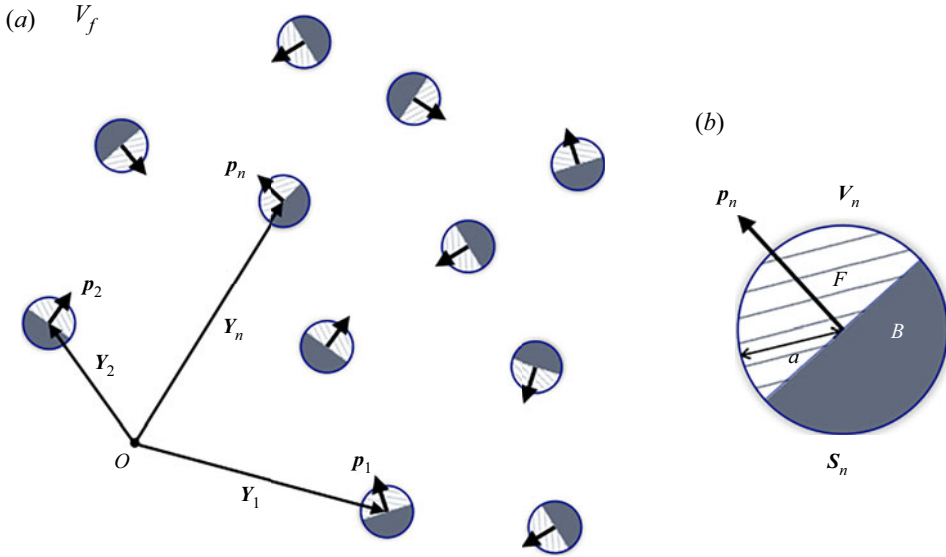


Figure 1. (a) Geometric description and parameter definition for (a) a reactive suspension system and (b) an individual active particle including the fluid domain V_f , as well the phoretic particle's position Y_n and orientation p_n , for radius a . The particle's orientation p_n , allows for the definition of its front caps (noted F and B respectively). The different colours of the caps (white or grey) illustrate their different chemical activities, while their patterns (striped and solid) illustrate their different mobilities.

on the surface of particle n :

$$-\mathbf{n} \cdot \nabla c = \alpha_n(\mathbf{n}) \quad \text{on } S_n, \tag{2.1}$$

where $\alpha_n(\mathbf{n})$ is the dimensionless activity distribution (i.e. emission rate) and \mathbf{n} is the outward normal unit vector on S_n . For sufficiently small particles, the solute's dynamics is purely diffusive, i.e. the relevant Péclet number $Pe = aU_0/D \ll 1$, so that c obeys Laplace's equation outside the particles,

$$\nabla^2 c = 0 \quad \text{in } V_f. \tag{2.2}$$

Together with an appropriate boundary conditions at the external boundary of V_f (e.g. $c \rightarrow 0$ for $|r| \rightarrow \infty$ in unbounded domains), these equations form a well-posed problem for the distribution of solute in the fluid domain V_f .

In response to a non-uniform solute distribution at the particles' surface, a phoretic slip flow \mathbf{u}_n^s develops outside a thin interaction layer (Anderson 1989) so that, effectively, the hydrodynamic boundary condition on S_n becomes

$$\mathbf{u} = \mathbf{U}_n + \boldsymbol{\Omega}_n \times \mathbf{r}_n + \mathbf{u}_n^s, \quad \text{with } \mathbf{u}_n^s = M_n(\mathbf{n}) \nabla_{\parallel} c \quad \text{on } S_n. \tag{2.3}$$

In the previous equation, $\nabla_{\parallel} = (\mathbf{I} - \mathbf{nn}) \cdot \nabla$ is the tangential gradient on the particle's surface, $\mathbf{r}_n = \mathbf{r} - \mathbf{Y}_n$ is the generic position relative to the centre of particle n and $M_n(\mathbf{n})$ denotes the dimensionless and spatially dependent phoretic mobility of the surface of particle n . For small particles, inertial effects are negligible (i.e. the relevant Reynolds number $Re = \rho U_0 a / \mu \ll 1$), and the dimensionless fluid's velocity and pressure (\mathbf{u}, p) satisfy the Stokes equations

$$\nabla p = \nabla^2 \mathbf{u}, \quad \nabla \cdot \mathbf{u} = 0 \quad \text{in } V_f, \tag{2.4a,b}$$

with an appropriate condition at the outer boundary of V_f (e.g. $\mathbf{u} \rightarrow 0$ for $|r| \rightarrow \infty$). Neglecting any outer forcing, such as gravity, each particle is hydrodynamically force and

torque free (Popescu *et al.* 2016) at all times,

$$\mathbf{F}_n = \int_{S_n} \boldsymbol{\sigma} \cdot \mathbf{n} \, dS = \mathbf{0}, \quad \mathbf{T}_n = \int_{S_n} \mathbf{r}_n \times (\boldsymbol{\sigma} \cdot \mathbf{n}) \, dS = \mathbf{0}, \quad (2.5a,b)$$

with $\boldsymbol{\sigma} = -p\mathbf{I} + (\nabla\mathbf{u} + \nabla\mathbf{u}^T)$ the dimensionless Newtonian stress tensor, and their dominant hydrodynamic signature is therefore that of a force dipole or stresslet \mathbf{S}_n (Batchelor 1970).

For a given concentration distribution c , (2.3)–(2.5a,b) form a well-posed problem for the fluid velocity and pressure, and particle velocities, so that, at a given time t , and for given particle positions and orientations, $\mathbf{Y}_n(t)$ and $\mathbf{p}_n(t)$, the successive Laplace and Stokes problems presented above uniquely determine the instantaneous particle velocities $\mathbf{U}_n(t)$ and $\boldsymbol{\Omega}_n(t)$, from which the motion of the particles is obtained

$$\frac{d\mathbf{Y}_n}{dt} = \mathbf{U}_n, \quad \frac{d\mathbf{p}_n}{dt} = \boldsymbol{\Omega}_n \times \mathbf{p}_n. \quad (2.6a,b)$$

For a single isolated particle, the Lorentz reciprocal theorem to Stokes flows provides the particle's translation and rotation velocities directly in terms of the phoretic slip (Stone & Samuel 1996)

$$\mathbf{U} = -\langle \mathbf{u}^s \rangle, \quad \boldsymbol{\Omega} = -\frac{3}{2a} \langle \mathbf{n} \times \mathbf{u}^s \rangle, \quad (2.7a,b)$$

where $\langle \cdot \rangle$ is the spatial average over the particle's surface. Similarly, the stresslet \mathbf{S} of the particle is obtained as (Lauga & Michelin 2016),

$$\mathbf{S} = -10\pi a^2 \langle \mathbf{n} \mathbf{u}^s + \mathbf{u}^s \mathbf{n} \rangle. \quad (2.8)$$

2.2. Hemispheric Janus phoretic particles

Most phoretic particles have a Janus-type surface consisting of two different materials or surface coatings with distinct physico-chemical properties (e.g. a catalytic side and a passive one) (Paxton *et al.* 2004; Howse *et al.* 2007; Theurkauff *et al.* 2012). These provide the particles with a built-in chemical asymmetry that triggers the inhomogeneity of the concentration distribution at their surface at the heart of their self-propulsion. In the following, we thus consider such hemispheric Janus particles with uniform but distinct mobilities (M_n^F, M_n^B) and activities (α_n^F, α_n^B) on their front (F) and back (B) hemispheres, as defined with respect to their orientation \mathbf{p}_n (figure 1b), e.g. the surface mobility of particle n writes

$$M_n(\mathbf{n}) = \bar{M}_n + M_n^* \text{sign}(\mathbf{p}_n \cdot \mathbf{n}), \quad (2.9)$$

with $\bar{M}_n = (M_n^F + M_n^B)/2$ and $M_n^* = (M_n^F - M_n^B)/2$ the mean mobility and mobility contrast, and a similar definition for the spatially dependent activity $\alpha_n(\mathbf{n})$ at the particle's surface. The special case of a particle with uniform mobility thus corresponds to $\bar{M}_n = M_n^0$ and $M_n^* = 0$.

3. An FCM-based method for phoretic suspensions

In the purely diffusive and viscous limit, solving for the particles' dynamics therefore amounts to solving sequentially two linear problems, namely a Laplace problem for c and a Stokes swimming problem for the hydrodynamic field and particles' velocity. Although the exact solution to this joint problem can be obtained analytically for the

single- and two-particle cases (Golestanian *et al.* 2007; Sharifi-Mood *et al.* 2016; Varma & Michelin 2019), analytical treatment becomes intractable beyond $N \geq 3$ due to the geometric complexity of the fluid domain, despite the problem's linearity. Numerical simulations are therefore critically needed, and several numerical strategies have been proposed recently and briefly reviewed in the introduction. In order to analyse accurately the collective dynamics of in a suspension of Janus phoretic particles, such a method must combine an efficient solution of the Laplace and Stokes problems outside a large number of finite-size objects, while providing accurate representation of the coupling at the surface of each particle between chemical and hydrodynamic fields.

With that double objective in mind, we propose and present here a novel numerical framework to solve for the reactive suspension problem presented in § 2, based on the classical FCM used for pure hydrodynamic simulations of passive particles or microswimmers, thereby generalizing its application to the solution of the chemical diffusion problem and its coupling with the already-established hydrodynamic FCM (Maxey & Patel 2001; Lomholt & Maxey 2003; Yeo & Maxey 2010; Delmotte *et al.* 2015). Section 3.1 develops the regularized Laplace problem and associated reactive FCM, while § 3.2 presents a brief review of the existing hydrodynamic FCM and § 3.3 combines both to obtain a new DFCM approach.

The fundamental idea of the FCM is to replace a solution of the Stokes equations only within the fluid domain V_f outside the forcing particles, by a solution of these equations over the entire domain $V_F = V_f \cup V_1 \cup \dots \cup V_N$ (i.e. both outside and inside the particles), replacing the surface boundary conditions with a distributed regularized forcing over a compact envelope calibrated so as to reproduce certain physical features of the problem and account for a weak form of the surface boundary conditions (figure 2). Doing so, the costly discrete resolution and time-dependent meshing of the particles is no longer necessary, so that efficient (e.g. spectral) Laplace and Stokes solvers on a fixed regular grid may be used at all times, offering significant performance and scalability advantages with respect to other approaches (e.g. boundary element methods). More specifically, FCM associates with each particle a finite set of regularized hydrodynamic singularities (force monopoles, dipoles and so on) chosen so as to satisfy a weak form of the surface boundary conditions.

3.1. Reactive FCM

We extend here this approach to the solution of the Laplace problem for c in (2.1) and (2.2). Replacing each particle by a distributed forcing modifies Laplace's equations into a Poisson equation over the entire domain V_F (including both fluid and particles),

$$\nabla^2 c = -g(\mathbf{r}, t) \quad \text{in } V_F, \tag{3.1}$$

where the function $g(\mathbf{r}, t)$ includes the source terms accounting for the presence of each particle.

3.1.1. Standard multiple expansion for Laplace problem

The exact solution of the Laplace problems can in fact be recovered from (3.1), when the function $g(\mathbf{r}, t)$ is taken as a (possibly infinite) set of singularities centred on each particle (Saffman 1973),

$$g(\mathbf{r}, t) = \sum_{n=1}^N [q_n^M \delta(\mathbf{r}_n) - \mathbf{q}_n^D \cdot \nabla \delta(\mathbf{r}_n) + \dots], \tag{3.2}$$

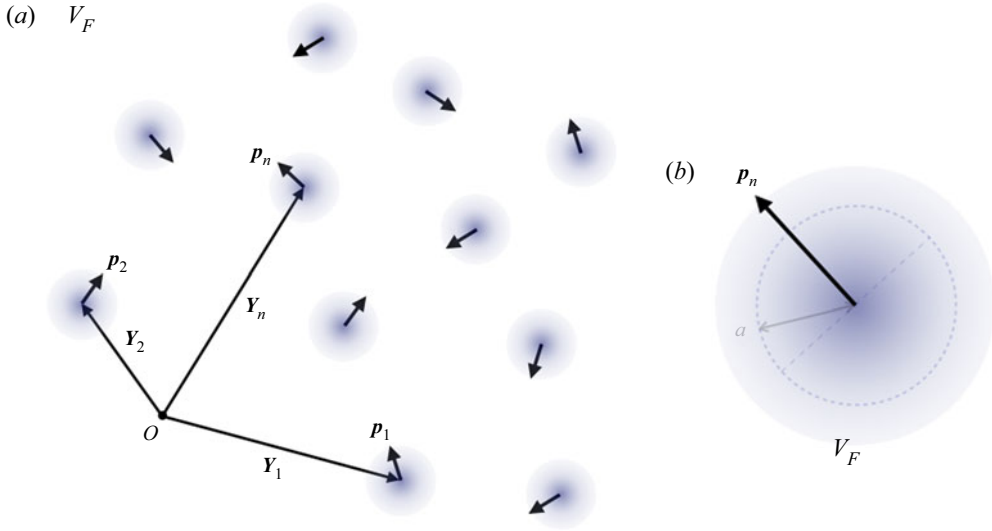


Figure 2. Regularized representation of (a) the reactive suspension system and (b) individual particles in the DFCM framework. The chemical and hydrodynamic fields are now defined over the entire domain with distributed forcings defined relative to each particle’s position Y_n and orientation p_n . The boundary S_n of the real particle (dashed) and its radius a are plotted only as reference.

where $\delta(r_n)$ is the Dirac delta distribution, and (q_n^M, q_n^D, \dots) are the intensities of the singularities associated with particle n , and are constant tensors of increasing order. Note that ∇ denotes here the gradient with respect to the observation position r and $r_n = r - Y_n$. This equation can be solved explicitly for the concentration field c as a multipole expansion for each particle in terms of source monopoles, dipoles, etc. . .

$$c(r, t) = \sum_{n=1}^N [q_n^M G^M(r_n) + q_n^D \cdot G^D(r_n) + \dots], \quad (3.3)$$

where G^M and G^D are the monopole and dipole Green’s functions and satisfy

$$\nabla^2 G^M = -\delta(r_n), \quad \nabla^2 G^D = \nabla \delta(r_n), \quad (3.4a,b)$$

together with appropriate decay or boundary conditions on the domain’s outer boundary. For unbounded domains with decaying conditions in the far field, the singular monopole and dipole Green’s functions are simply

$$G^M(r_n) = \frac{1}{4\pi r_n} \quad \text{and} \quad G^D(r_n) = -\nabla G^M = \frac{r_n}{4\pi r_n^3} \cdot \dots \quad (3.5a,b)$$

The concentration distributions associated with these singular Green’s functions are displayed in figure 3. Higher-order derivatives of $G^M(r)$, (3.5a,b), are also solutions of Laplace’s equation, leading to singularities of increasing order (quadrupole, octupole, . . .).

3.1.2. Truncated regularized multipole expansion

The previous approach, based on an infinite set of singular sources, is known as the standard multipole expansion of the Laplace problem. Although satisfying from a theoretical point of view, since it is able to recover an accurate representation of the

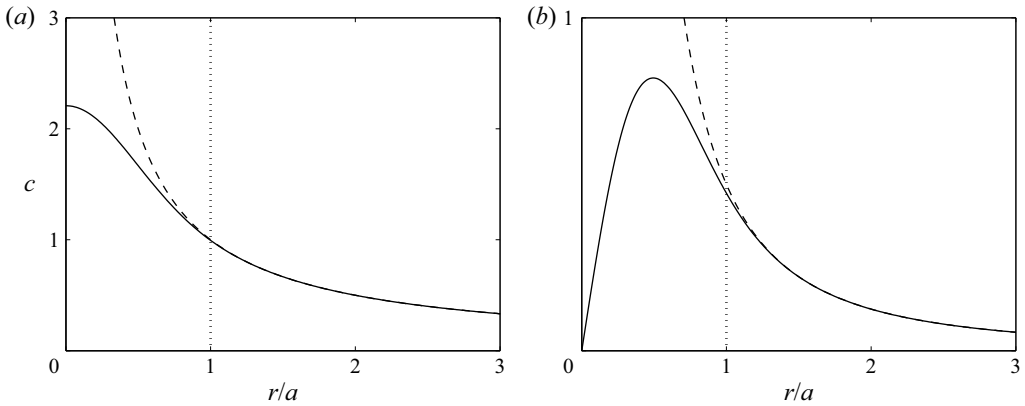


Figure 3. Singular (dotted lines, (3.5a,b)) and regularized (solid lines, (3.10)–(3.11)) concentration distributions along the axial polar direction associated with the Greens’ functions for the Laplace equation for (a) monopole terms and (b) dipole terms. The line $r/a = 1$ represents the particle surface.

analytical solution outside the particles for a large enough number of singular multipoles, it is not well suited for a versatile numerical implementation because of (i) the singular behaviour of the forcing terms in the modified Laplace equation, (3.1), and (ii) the *a priori* infinite set of singularities required for each particle.

To avoid the latter issue, the infinite expansion is truncated here after the first two terms, thus retaining the monopole and dipole contributions only. Physically, this amounts to retaining the two leading physical effects of the particle on the concentration field, i.e. a net emission with a front–back asymmetric distribution. In order to overcome the former problem, the standard FCM replaces the singular Dirac distributions $\delta(\mathbf{r})$ by regular Gaussian spreading functions $\Delta(\mathbf{r})$:

$$\Delta(\mathbf{r}) = (2\pi\sigma^2)^{-3/2} \exp\left(-\frac{r^2}{2\sigma^2}\right), \quad (3.6)$$

where σ denotes the finite-size support of this envelop and acts as a smoothing parameter of the method, thus eliminating the singular behaviour of the delta distribution $\delta(\mathbf{r})$ near the origin, thereby allowing for a more accurate numerical treatment. The original singular distribution is recovered when $\sigma \ll r$, i.e. the solution of the regularized problem is an accurate representation of the true solution away from the particle. This approach using regular distributions allows for a more versatile and robust numerical solution of the physical equations than their singular counterparts (Maxey & Patel 2001; Lomholt & Maxey 2003).

Combining these two approximations, we therefore consider a truncated regularized expansion including only the monopole and the dipole terms as

$$g(\mathbf{r}, t) = \sum_{n=1}^N [q_n^M \Delta^M(r_n) - \mathbf{q}_n^D \cdot \nabla \Delta^D(r_n)], \quad (3.7)$$

with the Gaussian spreading operators Δ^M and Δ^D defined as

$$\Delta^M(r) = (2\pi\sigma_M^2)^{-3/2} \exp\left(-\frac{r^2}{2\sigma_M^2}\right), \quad \Delta^D(r) = (2\pi\sigma_D^2)^{-3/2} \exp\left(-\frac{r^2}{2\sigma_D^2}\right), \quad (3.8a,b)$$

where M and D once again denote monopole and dipole, and σ_M and σ_D are the finite support of each regularized distribution and are free numerical parameters of the method that need to be calibrated. Note that, in general, these do not need to be identical (Lomholt & Maxey 2003).

The corresponding truncated regularized solution for c is then finally obtained as

$$c(\mathbf{r}, t) = \sum_{n=1}^N [q_n^M G^M(\mathbf{r}_n) + \mathbf{q}_n^D \cdot \mathbf{G}^D(\mathbf{r}_n)], \quad (3.9)$$

with the regularized monopole and dipole Green's functions

$$G^M(\mathbf{r}) = \frac{1}{4\pi r} \operatorname{erf}\left(\frac{r}{\sigma_M \sqrt{2}}\right), \quad (3.10)$$

$$\mathbf{G}^D(\mathbf{r}) = \frac{\mathbf{r}}{4\pi r^3} \left[\operatorname{erf}\left(\frac{r}{\sigma_D \sqrt{2}}\right) - \sqrt{\frac{2}{\pi}} \left(\frac{r}{\sigma_D}\right) \exp\left(-\frac{r^2}{2\sigma_D^2}\right) \right]. \quad (3.11)$$

These clearly match the behaviour of their singular counterpart, (3.5a,b), when r is greater than a few σ_M or σ_D , respectively, while still maintaining finite values within the particle (figure 3), e.g. $\mathbf{G}^D(\mathbf{r} = \mathbf{0}) = \mathbf{0}$.

3.1.3. Finding the intensity of the singularities

Up to this point, no information was implemented regarding the surface boundary conditions on c in (2.1). We now present how to determine the intensities of the monopole and dipole distributions associated with each particle, q_n^M and \mathbf{q}_n^D , so as to satisfy a weak form of the Neuman boundary condition, (2.1), i.e. its first two moments over the particle's surface. Using the multipole expansion of the fundamental integral representation of the concentration (see Appendix A), the monopole and dipole intensities of particle n , q_n^M and \mathbf{q}_n^D , are obtained as (Yan & Brady 2016)

$$q_n^M = \int_{S_n} \alpha_n dS, \quad \mathbf{q}_n^D = a \int_{S_n} \alpha_n \mathbf{n} dS + 4\pi a^2 \langle c\mathbf{n} \rangle_n, \quad (3.12a,b)$$

where the second term in \mathbf{q}_n^D is proportional to the concentration polarity at the surface of particle n , i.e. its first moment $\langle c\mathbf{n} \rangle_n$, and is defined using the surface average operator $\langle \cdot \rangle_n$ over the surface of particle n . Note that the activity distribution at the particle's surface is known, and thus (2.9) explicitly provides the monopole intensity and the first term in the dipole intensity. The second contribution to the latter requires, however, knowledge of the solution on the particle's surface – which is not explicitly represented in the present FCM approach. This term therefore requires to be solved for as part of the general problem. In the previous equation, it should be noted that the dimensionless particle radius is $a = 1$, but will be kept in the equations to emphasize the relative scaling of the numerical spreading envelopes (e.g. σ_M and σ_D) with respect to the particle size.

Here, we use an iterative approach to solve this linear joint problem for the dipole intensity and concentration field, solving alternatively (3.7) and (3.12a,b) until convergence is reached, as defined by the following criterion between two successive

iterations:

$$\left\| \frac{\langle c\mathbf{n} \rangle^{k+1} - \langle c\mathbf{n} \rangle^k}{\langle c\mathbf{n} \rangle^{k+1}} \right\|_{\infty} < \epsilon, \quad (3.13)$$

where $\langle c\mathbf{n} \rangle^k$ is the vector collecting the polarities of the N particles at iteration k . For the results presented in this work, we set the tolerance to $\epsilon = 10^{-10}$ in our calculations.

3.1.4. Regularized moments of the concentration distribution

Finding the dipole intensity, q_n^D , requires computing the polarity $\langle c\mathbf{n} \rangle_n$, which is in principle defined at the particle's surface. To follow the spirit of FCM, and allow for efficient numerical treatment, this surface projection is replaced by a weighted projection over the entire volume V_F

$$\langle c\mathbf{n} \rangle_n = \frac{1}{4\pi a^2} \int_{S_n} c \mathbf{n} dS \quad \rightarrow \quad \{c\mathbf{n}\}_n = \int_{V_F} c \mathbf{n}_n \Delta^P(\mathbf{r}_n) dV, \quad (3.14)$$

with \mathbf{n}_n now defined as $\mathbf{n}_n = \mathbf{r}_n/r_n$, and the regular averaging kernel Δ^P for the polarity as

$$\Delta^P(\mathbf{r}) = \frac{r}{8\pi\sigma_P^4} \exp\left(-\frac{r^2}{2\sigma_P^2}\right). \quad (3.15)$$

Beyond its importance for determining the dipole intensity associated with a given particle, we will later show that the polarity of the concentration at the surface of particle n is directly related to its self-induced phoretic velocity, (2.7a,b), and that, similarly, the self-induced hydrodynamic stresslet signature of the particle is in general associated with the first two moments of the surface concentration. Similarly to the polarity, the second surface moment, $\langle c(\mathbf{nn} - \mathbf{I}/3) \rangle_n$ will be replaced in our implementation by a weighted volume projection $\{c(\mathbf{nn} - \mathbf{I}/3)\}_n$

$$\begin{aligned} \langle c(\mathbf{nn} - \mathbf{I}/3) \rangle_n &= \frac{1}{4\pi a^2} \int_{S_n} c \left(\mathbf{nn} - \frac{\mathbf{I}}{3} \right) dS \rightarrow \{c(\mathbf{nn} - \mathbf{I}/3)\}_n \\ &= \int_{V_F} c \left(\mathbf{n}_n \mathbf{n}_n - \frac{\mathbf{I}}{3} \right) \Delta^S(\mathbf{r}_n) dV, \end{aligned} \quad (3.16)$$

where the projection kernel for the second moment of concentration, Δ^S , is defined as

$$\Delta^S(\mathbf{r}) = \frac{r^2}{3(2\pi)^{3/2}\sigma_S^5} \exp\left(-\frac{r^2}{2\sigma_S^2}\right). \quad (3.17)$$

The envelopes σ_P and σ_S are free parameters in the method that need to be calibrated. In our reactive FCM formulation, we use modified forms of the Gaussian operator Δ as projection operators, (3.15) and (3.17), in order to ensure a fast numerical convergence of the integration for the first and second moment calculations, (3.14) and (3.16) respectively. The integrals over the entire volume V_F of these averaging functions is still equal to one, and their weight is shifted from the particle centre toward the particle surface (figure 4), which is both numerically more accurate and more intuitive physically as these operators are used to obtain the properties of the particle on its surface.

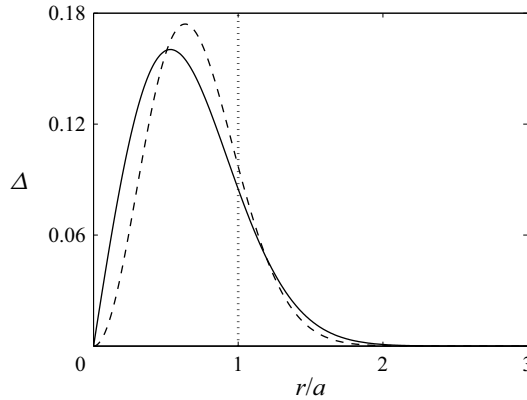


Figure 4. Averaging envelopes for the first and second moments of concentration, Δ^P (solid, (3.15)) and Δ^S (dashed, (3.17)) respectively. The numerical values for σ_P and σ_S are set from (3.21a,b) and (3.24).

3.1.5. Calibrating the spreading/averaging envelopes

Our method relies on four numerical parameters (σ_M , σ_D , σ_P , σ_S) that we choose to calibrate so as to ensure that several key results in reference configurations are obtained exactly. In particular, to properly account for the phoretic drift induced by the other particles, we ensure that the polarity $\langle c\mathbf{n} \rangle$ of an isolated particle placed in an externally imposed uniform gradient of concentration can be exactly recovered using the regular representation and averaging operators. A similar approach is then followed for the particle's second moment of concentration $\langle c(\mathbf{nn} - \mathbf{I}/3) \rangle$ in a quadratic externally imposed field.

Isolated passive particle in an external linear field – We first consider a single particle placed at the origin in an externally imposed linear concentration field so that for $r \gg a$, $c \approx c_E$ with

$$c_E = \mathbf{L}_E \cdot \mathbf{r}, \tag{3.18}$$

where \mathbf{L}_E is the externally imposed uniform gradient. For a passive particle (i.e. $\alpha = 0$), satisfying the boundary condition, (2.1), at the surface of the particle imposes that the exact concentration distribution around the particle is $c = c_E + c_I^o$, with $c_I^o(\mathbf{r}) = a^3 \mathbf{L}_E \cdot \mathbf{r} / (2r^3)$ a singular dipole-induced field. The polarity of the external and induced parts, c_E and c_I , can be obtained analytically as

$$\langle c_E \mathbf{n} \rangle = \frac{a}{3} \mathbf{L}_E, \quad \langle c_I^o \mathbf{n} \rangle = \frac{a}{6} \mathbf{L}_E. \tag{3.19a,b}$$

Following the framework presented above, the regularized solution can be written $c = c_E + c_I^r$ with c_I^r a regularized dipole, and the corresponding regularized-volume moments based on (3.14) are obtained using (3.11), as

$$\langle c_E \mathbf{n} \rangle = \sqrt{\frac{\pi}{8}} \sigma_P \mathbf{L}_E, \quad \langle c_I^r \mathbf{n} \rangle = \frac{a^3 \sigma_P}{12(\sigma_D^2 + \sigma_P^2)^{3/2}} \mathbf{L}_E. \tag{3.20a,b}$$

Identification of the regularized result (3.20a,b) with the true solution (3.19a,b), determines σ_P and σ_D uniquely as

$$\frac{\sigma_P}{a} = \frac{1}{3} \sqrt{\frac{8}{\pi}} \approx 0.5319, \quad \frac{\sigma_D}{a} = \sqrt{\left(\frac{\sigma_P}{2a}\right)^{2/3} - \left(\frac{\sigma_P}{a}\right)^2} \approx 0.3614. \tag{3.21a,b}$$

Isolated passive particle in an external quadratic field – Similarly, in an external quadratic field c_E of the form

$$c_E(\mathbf{r}) = \mathbf{r} \cdot \mathbf{Q}_E \cdot \mathbf{r}, \quad (3.22)$$

with \mathbf{Q}_E a second-order symmetric and traceless tensor, the concentration distribution around a passive particle ($\alpha = 0$) takes the form $c = c_E + c_I^o$ with $c_I^o(\mathbf{r})$ an induced singular quadrupole. The exact and regularized second moments of the external field c_E at the particle surface are equal to

$$\langle c_E(\mathbf{nn} - I/3) \rangle = \frac{2a^2}{15} \mathbf{Q}_E, \quad \{c_E(\mathbf{nn} - I/3)\} = \frac{2\sigma_S^2}{3} \mathbf{Q}_E. \quad (3.23a,b)$$

Identifying both results determines the size of the averaging envelope for the second moment uniquely, as

$$\frac{\sigma_S}{a} = \sqrt{\frac{1}{5}} \approx 0.4472. \quad (3.24)$$

Note that we do not enforce here a constraint on the representation of the second moment of the induced field c_I , since the particles' representations do not include a regularized quadrupole in our method.

The value σ_M remains as a free parameter at this point and cannot be calibrated with a similar approach. In the following, in order to minimize the number of distinct numerical parameters and to minimize the departure of the regularized solution from its singular counterpart, we set its value equal to the smallest envelope size, namely $\sigma_M = \sigma_D$. These specific values of the parameters were used in figures 3 and 4.

3.2. Hydrodynamic FCM

To compute the hydrodynamic interactions between phoretic particles, we rely on the FCM. This section briefly describes the existing FCM framework developed for the simulation of passive and active suspensions in Stokes flow.

3.2.1. FCM for passive suspensions

With hydrodynamic FCM, the effect of the particles on the fluid is accounted for through a forcing term \mathbf{f} applied to the dimensionless Stokes equations

$$\nabla p - \nabla^2 \mathbf{u} = \mathbf{f}(\mathbf{r}, t) \quad \text{in } V_F. \quad (3.25)$$

As for reactive FCM, this forcing arises from a truncated regularized multipolar expansion up to the dipole level

$$\mathbf{f}(\mathbf{r}, t) = \sum_{n=1}^N [\mathbf{F}_n \Delta(r_n) + \mathbf{D}_n \cdot \nabla \Delta^*(r_n)], \quad (3.26)$$

where the spreading envelopes are defined by

$$\Delta(r) = (2\pi\sigma^2)^{-3/2} \exp\left(-\frac{r^2}{2\sigma^2}\right), \quad \Delta^*(r) = (2\pi\sigma_*^2)^{-3/2} \exp\left(-\frac{r^2}{2\sigma_*^2}\right). \quad (3.27a,b)$$

Here, \mathbf{F}_n and \mathbf{D}_n are the force monopole and dipole applied to particle n . The force dipole can be split into a symmetric part, the stresslet \mathbf{S} , and an antisymmetric one related to the

external torque T

$$\mathbf{D}_n = \mathbf{S}_n + \frac{1}{2}\boldsymbol{\epsilon} \cdot T_n, \quad (3.28)$$

with $\boldsymbol{\epsilon}$ the third-order permutation tensor. The corresponding regularized solution for the fluid velocity \mathbf{u} is then obtained as

$$\mathbf{u} = \mathbf{u}(\mathbf{r}) = \sum_{n=1}^N [\mathbf{F}_n \cdot \mathbf{J}(\mathbf{r}_n) + \mathbf{D}_n : \mathbf{R}^*(\mathbf{r}_n)]. \quad (3.29)$$

For unbounded domains with vanishing perturbations in the far field (i.e. $\|\mathbf{u}\| \rightarrow 0$ when $r \rightarrow \infty$), the regularized Green's function $\mathbf{J}(\mathbf{r})$ reads

$$\mathbf{J}(\mathbf{r}) = \frac{1}{8\pi r} \left(A(r)\mathbf{I} + B(r)\frac{\mathbf{r}\mathbf{r}}{r^2} \right), \quad (3.30)$$

with

$$A(r) = \left(1 + \frac{\sigma^2}{r^2} \right) \operatorname{erf} \left(\frac{r}{\sigma\sqrt{2}} \right) - \frac{\sigma}{r} \sqrt{\frac{2}{\pi}} \exp \left(-\frac{r^2}{2\sigma^2} \right), \quad (3.31)$$

$$B(r) = \left(1 - \frac{3\sigma^2}{r^2} \right) \operatorname{erf} \left(\frac{r}{\sigma\sqrt{2}} \right) + \frac{3\sigma}{r} \sqrt{\frac{2}{\pi}} \exp \left(-\frac{r^2}{2\sigma^2} \right), \quad (3.32)$$

and $\mathbf{R}^* = \nabla \mathbf{J}^*$ is the FCM dipole Green's function evaluated with the parameter σ_* .

The particle's translational and angular velocities, \mathbf{U}_n and $\boldsymbol{\Omega}_n$, are obtained from a volume-weighted average of the local fluid velocity and vorticity

$$\mathbf{U}_n = \int_{V_F} \mathbf{u} \Delta(\mathbf{r}_n) dV, \quad \boldsymbol{\Omega}_n = \frac{1}{2} \int_{V_F} [\nabla \times \mathbf{u}] \Delta^*(\mathbf{r}_n) dV. \quad (3.33a,b)$$

The Gaussian parameters, σ and σ^* , are calibrated to recover the correct Stokes drag, $\mathbf{F} = 6\pi a \mu \mathbf{U}$, and viscous torque, $\mathbf{T} = 8\pi a^3 \mu \boldsymbol{\Omega}$, of an isolated particle (Maxey & Patel 2001; Lomholt & Maxey 2003), leading to

$$\frac{\sigma}{a} = \frac{1}{\sqrt{\pi}} \approx 0.5641, \quad \frac{\sigma^*}{a} = \frac{1}{(6\sqrt{\pi})^{1/3}} \approx 0.4547. \quad (3.34a,b)$$

The rigidity of the particle is similarly weakly enforced by imposing that the volume-averaged strain rate \mathbf{E}_n over the envelope of particle n vanishes

$$\mathbf{E}_n = \frac{1}{2} \int_{V_F} [\nabla \mathbf{u} + (\nabla \mathbf{u})^T] \Delta^*(\mathbf{r}_n) dV = \mathbf{0}, \quad (3.35)$$

which determines the stresslet \mathbf{S}_n induced by particle n . Note that, unlike forces and torques which are typically set by external or inter-particle potentials, the stresslets result from the constraint on the flow given by (3.35) and, consequently, need to be solved for as part of the general flow problem. The resulting linear system for the unknown stresslet coefficients is solved directly or iteratively, with the conjugate gradients method, depending on the number of particles considered (Lomholt & Maxey 2003; Yeo & Maxey 2010). In the following, we consider pairs of particles (see § 4) and therefore use direct inversion.

Note that the averaging envelopes used to recover the translational and rotational velocities, Δ_n and Δ_n^* , are exactly the same as the spreading operators in (3.26),

all of them Gaussian functions. As a result, the spreading and averaging operators are adjoints to one another. Also note that only two envelope lengths are required for the hydrodynamic problem: σ and σ_* . In contrast, the new reactive FCM extension presented in § 3.1 uses spreading and averaging operators that are not adjoint. To recover the first (3.14) and second (3.16) moments of concentration we have two non-Gaussian averaging envelopes (Δ^P and Δ^S), that differ from the Gaussian spreading envelopes (Δ^M and Δ^D) in (3.7). While having adjoint operators is crucial in hydrodynamic FCM to satisfy the fluctuation–dissipation balance, the lack of adjoint properties for the Laplace problem does not raise any issue in the deterministic setting.

3.2.2. Active hydrodynamic FCM

In recent years, FCM has been extended to handle suspensions of active particles, such as microswimmers. In addition to undergoing rigid body motion in the absence of applied forces or torques, active and self-propelled particles are also characterized by the flows they generate. These flows can be incorporated into FCM by adding an appropriate set of regularized multipoles to the Stokes equations. This problem was solved previously for the classical squirmer model (Delmotte *et al.* 2015), a spherical self-propelled particle that swims using prescribed distortions of its surface. In the most common case where radial distortions are ignored, the squirmer generates a tangential slip velocity on its surface, just like phoretic particles, which can be expanded into spherical harmonics modes (Blake 1971; Pak & Lauga 2014). Consistently with the phoretic problem presented above, only the first two modes are included in the following.

The FCM force distribution produced by N microswimmers self-propelling with a surface slip velocity is given by

$$\mathbf{f}(\mathbf{r}, t) = \sum_{n=1}^N [\mathbf{S}_n \cdot \nabla \Delta^*(r_n) + \mathbf{S}_n^a \cdot \nabla \Delta(r_n) + \mathbf{H}_n^a \nabla^2 \Delta^*(r_n)], \quad (3.36)$$

where \mathbf{S}_n^a is the active stresslet and \mathbf{H}_n^a is the active potential dipole associated with the swimming disturbances of swimmer n . The latter is defined as

$$\mathbf{H}_n^a = -2\pi a^3 \mathbf{U}_n^a, \quad (3.37)$$

where \mathbf{U}_n^a is the swimming velocity arising from the slip velocity on the swimmer surface \mathbf{u}^s (2.7a,b). Note that the rigidity stresslet \mathbf{S}_n is included in (3.36) to enforce the absence of deformation of the swimmers, (3.35). The resulting velocity field reads

$$\mathbf{u}(\mathbf{r}, t) = \sum_{n=1}^N [\mathbf{S}_n : \mathbf{R}^*(r_n) + \mathbf{S}_n^a : \mathbf{R}(r_n) + \mathbf{H}_n^a \cdot \mathbf{A}^*(r_n)], \quad (3.38)$$

where \mathbf{R} is the FCM dipole Green’s function evaluated with the parameter σ instead of σ_* . The second-order tensor \mathbf{A}^* is the FCM Green’s function for the potential dipole

$$\mathbf{A}^*(\mathbf{r}) = \frac{1}{4\pi r^3} \left[\mathbf{I} - \frac{3\mathbf{r}\mathbf{r}}{r^2} \right] \operatorname{erf} \left(\frac{r}{\sigma_* \sqrt{2}} \right) - \frac{1}{\mu} \left[\left(\mathbf{I} - \frac{\mathbf{r}\mathbf{r}}{r^2} \right) + \left(\mathbf{I} - \frac{3\mathbf{r}\mathbf{r}}{r^2} \right) \left(\frac{\sigma_*}{r} \right)^2 \right] \Delta^*(r). \quad (3.39)$$

The particles' velocity, angular velocity and mean strain rate are then computed as

$$U_n = U_n^a - W_n + \int_{V_F} \mathbf{u} \Delta(r_n) dV, \quad (3.40)$$

$$\Omega_n = \Omega_n^a + \frac{1}{2} \int_{V_F} [\nabla \times \mathbf{u}] \Delta^*(r_n) dV, \quad (3.41)$$

$$\mathbf{E}_n = -\mathbf{K}_n + \frac{1}{2} \int_{V_F} [\nabla \mathbf{u} + (\nabla \mathbf{u})^T] \Delta^*(r_n) dV = \mathbf{0}, \quad (3.42)$$

where the active swimming velocities U_n^a and rotation rates Ω_n^a correspond to the intrinsic velocities of particle n , if it was alone (i.e. in the absence of external flows or other particles), and W_n and \mathbf{K}_n are defined as

$$W_n = \int_{V_F} [H_n^a \cdot \mathbf{A}^*(r_n)] \Delta(r_n) dV, \quad (3.43)$$

$$\mathbf{K}_n = \frac{1}{2} \int_{V_F} [\mathbf{S}_n^a : \nabla \mathbf{R}(r_n) + (\mathbf{S}_n^a : \nabla \mathbf{R}(r_n))^T] \Delta^*(r_n) dV, \quad (3.44)$$

and are included to subtract away the spurious self-induced velocities and local rates of strain arising from the integration of the full velocity field \mathbf{u} , which already includes the contribution of H_n^a and \mathbf{S}_n^a (Delmotte *et al.* 2015).

3.3. Diffusio-phoretic FCM

At this point, we have described our new reactive FCM framework and have reviewed the key aspects of the existing active hydrodynamic FCM. These two steps provide respectively the solution (i) for the concentration field and its moments at the surface of each particle in terms of their position and orientation, and (ii) the particles' velocity in terms of their active hydrodynamic characteristics, i.e. their intrinsic velocities and stresslet, U_n^a , Ω_n^a and \mathbf{S}_n^a . To solve for the full diffusio-phoretic problem (i.e. obtain the velocity of the particle in terms of their position and orientation), these quantities must be determined from the chemical environment of the particles. The following section details how to obtain these active characteristics from the output of the reactive problem and provides algorithmic details on the numerical implementation. This new diffusio-phoretic framework based on the FCM is referred to as DFCM hereafter.

3.3.1. DFCM: coupling reactive and hydrodynamic FCM

The active swimming speed U_n^a involved in the potential dipole H_n^a (3.37), is the phoretic response of particle n to the chemical field, if it was hydrodynamically isolated (i.e. neglecting the presence of other particles in solving the swimming problem). It thus includes its self-induced velocity (i.e. the response to the concentration contrasts induced by its own activity) and the drift velocity induced by the activity of the other particles. The swimming problem for a hydrodynamically isolated particle in unbounded flows can be solved directly using the reciprocal theorem (Stone & Samuel 1996), and using the definition of the phoretic slip flow

$$U_n^a = -\langle \mathbf{u}^s \rangle_n = -\langle M \nabla_{\parallel} c \rangle_n. \quad (3.45)$$

After substitution of the mobility distribution at the surface of particle n , (2.9), using a truncated multipolar expansion of the surface concentration on particle n (up to

its second-order moment) and integration by parts, the intrinsic swimming velocity is obtained in terms of the first two surface concentration moments (see Appendix B for more details)

$$U_n^a = -\frac{2\bar{M}_n}{a}\langle cn \rangle_n - \frac{15M_n^*}{8a}[2\langle c(\mathbf{nn} - I/3) \rangle_n \cdot \mathbf{p}_n + (\langle c(\mathbf{nn} - I/3) \rangle_n : \mathbf{p}_n \mathbf{p}_n) \mathbf{p}_n]. \quad (3.46)$$

Similarly, the active stresslet \mathbf{S}_n^a , is defined as in (2.8),

$$\mathbf{S}_n^a = -10\pi a^2 \langle \mathbf{nu}^s + \mathbf{u}^s \mathbf{n} \rangle_n = -10\pi a^2 \langle M(\mathbf{n}\nabla_{\parallel} c + (\nabla_{\parallel} c)\mathbf{n}) \rangle_n, \quad (3.47)$$

and rewrites in terms of the moments of concentration (see Appendix B for more details)

$$\mathbf{S}_n^a = -60\pi a \bar{M}_n \langle c(\mathbf{nn} - I/3) \rangle_n + \frac{15\pi a M_n^*}{2} [\langle (cn)_n \cdot \mathbf{p}_n \rangle (I - \mathbf{p}_n \mathbf{p}_n) - \langle cn \rangle_n \mathbf{p}_n - \mathbf{p}_n \langle cn \rangle_n]. \quad (3.48)$$

Finally, the active rotation $\boldsymbol{\Omega}_n^a$, (2.7a,b), is obtained in terms of the moments of concentration and the mobility contrast (see Appendix B)

$$\boldsymbol{\Omega}_n^a = -\frac{9M_n^*}{4a^2} \mathbf{p}_n \times \langle cn \rangle_n. \quad (3.49)$$

For uniform mobility, the swimming velocity and stresslet are directly related to the first and second of surface concentrations, but non-uniform mobility introduces a coupling of the different concentration moments. Here, the surface concentration is expanded up to its second-order moment only.

In our regularized approach, the surface concentration moments appearing in the previous equations will conveniently be computed as weighted volume averages over the entire domain V_F as detailed in (3.14) and (3.16).

Computing the second moment of concentration, however, requires an additional step: as detailed in § 3.1.5, the second moment of concentration in an external field arises from the second gradient of that external field, and includes both an externally induced component $\langle c_E(\mathbf{nn} - I/3) \rangle_n$ (i.e. the moment of that externally imposed field) and a self-induced component which corresponds to the second moment of the induced field generated by the particle to ensure that the correct flux boundary condition is satisfied at the particles' surface. For a chemically inert particle ($\alpha = 0$), the self-induced contribution is obtained exactly as $\langle c_I^o(\mathbf{nn} - I/3) \rangle_n = \frac{2}{3} \langle c_E(\mathbf{nn} - I/3) \rangle_n$.

Our representation of the particles in the chemical problem is, however, truncated at the dipole level, (3.9), and as a result, the quadrupolar response of the particle to the external field cannot be accounted for directly. To correct for this shortcoming, we first compute the external second moment produced by the other particles on particle n using (3.16) and (3.9), and multiply the resulting value by 5/3 to account for the full second moment induced by the concentration field indirectly.

Finally, the particles are themselves active and may generate an intrinsic quadrupole. Its effect on the second surface concentration moment can be added explicitly in terms of the second activity moment, so that the total second moment on particle n is finally evaluated as

$$\langle c(\mathbf{nn} - I/3) \rangle_n = \frac{5}{3} \langle c_E(\mathbf{nn} - I/3) \rangle_n + \frac{a}{D} \langle \alpha(\mathbf{nn} - I/3) \rangle_n. \quad (3.50)$$

In summary, at a given time step, the particles' velocities are obtained from their instantaneous position and orientation as follows. The first two surface concentration

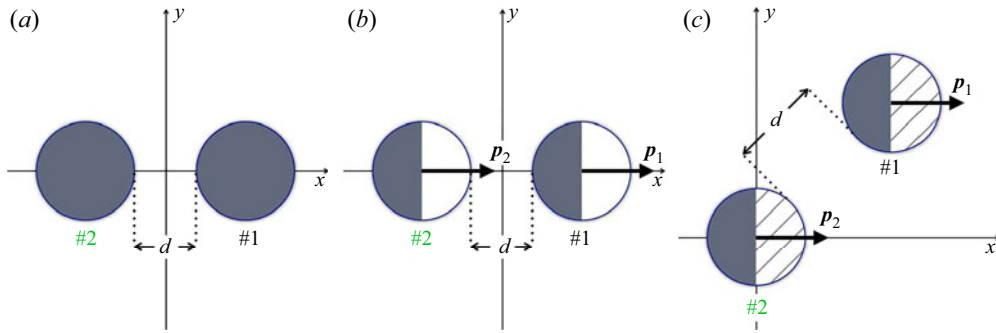


Figure 5. Validation cases considered. (a) Case A, isotropic particles with uniform mobility, (b) Case B, hemispheric Janus particles with uniform mobility, (c) Case C, hemispheric Janus particles with non-uniform mobility. In each case, both particles have exactly the same orientation and phoretic properties and their dimensionless separation is denoted by d .

moments are first obtained using our new reactive FCM framework by solving the Poisson problem (3.7). These moments are then used to compute the phoretic intrinsic translation and rotation velocities (3.46) and (3.49), as well as the active stresslets and potential dipoles (3.48) and (3.37). The Stokes equations forced by the swimming singularities (3.36), and subject to the particle rigidity constraint (3.42), are finally solved to obtain the total particle velocities (3.40) and (3.41).

3.3.2. Numerical details

The volume integrals required to compute the concentration moments and the hydrodynamic quantities are performed with a Riemann sum on Cartesian grids centred at each particle position. To ensure a sufficient resolution, the grid size, Δx , is chosen so that the smallest envelope size σ_D satisfies $\sigma_D = 1.5\Delta x = 0.3614a$, which corresponds to approximately 4 grid points per radius. Owing to the fast decay of the envelopes, the integration domain is truncated so that the widest envelope (that with the largest σ) essentially vanishes on the boundary of the domain, $\Delta(r) < \gamma = 10^{-16}$, which, given the grid resolution, requires 39 integration points in each direction. Doing so, the numerical integrals yield spectral accuracy. Setting instead $\gamma = \epsilon = 10^{-10}$, where ϵ is the relative tolerance for the polarity in the iterative procedure (3.13), reduces that number to 31 integration points along each axis while maintaining spectral convergence.

4. Results

In this section, we evaluate the accuracy of the present novel DFCM framework in three different canonical or more generic configurations involving pairs of isotropic and Janus phoretic particles, as shown in figure 5. The particles' motions are restricted to a plane within a three-dimensional unbounded domain for the sake of clarity in visualizing the results.

In this validation process, DFCM is compared to three existing methods providing either a complete or approximate solution of the problem. The simplest one, the far-field approximation model (Soto & Golestanian 2014; Varma & Michelin 2019), relies on a multipolar expansion of the reactive and hydrodynamic singularities up to the dipole level generated by each particle, but neglects the finite size of the particles (i.e. without reflections on the polarity and rigidity stresslet). Our results are also compared to the

complete (exact) solution of the problem (i.e. solving the complete hydrodynamic and chemical fields regardless of the particles' distance, accounting for their finite size). For axisymmetric problems, this solution is obtained semi-analytically using the bi-spherical coordinates approach (Michelin & Lauga 2015; Reigh & Kapral 2015), whose accuracy is only limited by the number of Legendre modes used to represent the solution. For non-axisymmetric configurations, the complete solution is obtained numerically using the regularized boundary element method (Montenegro-Johnson *et al.* 2015). These reference solutions are referred to in the following, as FFA, BSC and BEM respectively.

4.1. Isotropic particles – axisymmetric configuration

The first configuration, Case A (figure 5a), consists of two identical isotropic particles with uniform activity and mobility ($\alpha_n^F = \alpha_n^B = 1$, $M_n^F = M_n^B = 1$) separated by a distance d along the x -axis (Varma *et al.* 2018; Nasouri & Golestanian 2020b). Phoretic particles require an asymmetry in their surface concentration to self-propel (Golestanian *et al.* 2007), so that an isolated isotropic particle cannot swim. In the configuration considered here, however, the concentration gradient produced by a second isotropic particle introduces the required asymmetry to generate motion along the x -axis.

Figure 6(a) shows the concentration field induced by two isotropic particles for $d = 1$. The DFCM solution (upper half) is in good agreement with BSC (lower half), except near the particles' boundaries in the gap, where the low-order multipolar expansion of DFCM and inaccurate resolution of the particle's surface underestimate the concentration field. The increase in concentration between the particles is a direct result of the confinement between their active surfaces. It produces a surface concentration gradient and phoretic slip flow on each particle's boundary that pumps the fluid toward this high concentration zone and thus drives the particles away from each other (figure 6d). This effect is magnified as d is reduced, leading to higher particle velocities and higher moments of concentration for shorter distances.

The evolution with interparticle distance of the particles' polarity, a measure of the net concentration gradient over their surface, is shown on figure 6(b) as obtained with the DFCM, BSC and FFA approaches. While both FFA and DFCM are in good agreement with the exact solution (BSC) even for relatively small distances, the DFCM approach provides a noticeable improvement over the cruder representation of FFA in the near field ($d < 1$), where the iterative corrections for the mutually induced polarity (3.13) contribute significantly. The expected decay of the polarity as $1/d^2$ is recovered (figure 6(b), inset) in all three cases as the dominant contribution to the polarity is proportional to the gradient of the leading-order monopolar concentration field. Similar results are obtained for the second moment of concentration (figure 6c), with an expected $1/d^3$ -decay proportional to the second gradient of the leading order concentration field. We note that isotropic particles do not drive any flow when isolated (and therefore do not have any hydrodynamic signature), but acquire a net stresslet as a result of their chemical interactions, behaving as pusher swimmers.

The resulting translational velocities are shown in figure 6(d) where, again, DFCM performs better than FFA in the range $d < 2$ since it additionally considers the hydrodynamic interactions of the particles (e.g. the effect of the rigidity constraint through the rigidity stresslet, see (3.36)), in addition to the active flows, while FFA does not. Such discrepancy arises from the accumulated errors in the successive truncated multipolar expansions; using the BSC solution as a reference, we can determine that for near-field interactions of the two particles, approximately 25%–30% of the DFCM error comes

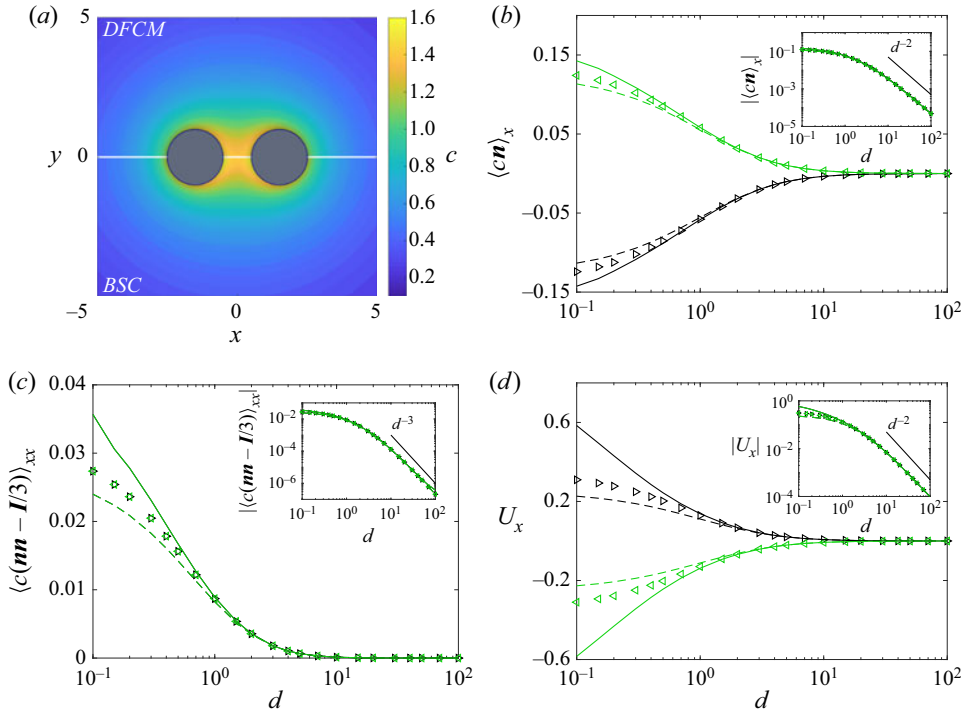


Figure 6. Case A. (a) Concentration field for $d = 1$ (upper half: DFCM, lower half: BSC), (b) first moment of concentration $\langle cn \rangle_x$, (c) second moment of concentration $\langle c(nn - I/3) \rangle_{xx}$, (d) velocity U_x . The black lines (and markers) correspond to particle 1 and the light green ones to particle 2. The triangle markers correspond to DFCM, the solid lines correspond to BSC, while the dashed lines to FFA. The inset shows the absolute values in logarithmic scale and the corresponding decay. The surface averages $\langle \dots \rangle$ were used for BSC and FFA, while the volume average $\{ \dots \}$ was used for DFCM. All the omitted components of $\langle cn \rangle$, $\langle c(nn - I/3) \rangle$ and U are zero.

from the reactive FCM approximation (3.7), while the other 70%–75% comes from the hydrodynamical FCM approximation (3.36). As expected, in the far-field limit, the velocity decays as $1/d^2$ since it is proportional to the polarity to leading order and this dominant contribution does not involve any hydrodynamic interactions; these would correspond at leading order to the contribution of the stresslet generated by the presence of the other particles and decay as $1/d^5$ (Varma & Michelin 2019).

4.2. Janus particles – axisymmetric configuration

Our second configuration of interest, Case B (figure 5b), focuses on Janus particles, which are currently the most commonly used configuration for self-propelled phoretic particle in both experiments and theoretical models. Their motion stems from the self-induced concentration gradients produced by the difference in activity between their two hemispheres. Here, we consider two identical Janus particles with uniform mobility ($M_n^F = M_n^B = 1$), a passive front cap ($\alpha_n^F = 0$) and an active back cap ($\alpha_n^B = 1$), leading to a self-propulsion velocity of $U^\infty = \frac{1}{4}e_x$ (Golestanian *et al.* 2007). We further focus here on an axisymmetric setting where the particles’ orientation coincides with the line connecting their centres, for which an exact semi-analytic solution of the complete hydrochemical problem is available using bispherical coordinates (BSC) as exploited in several recent

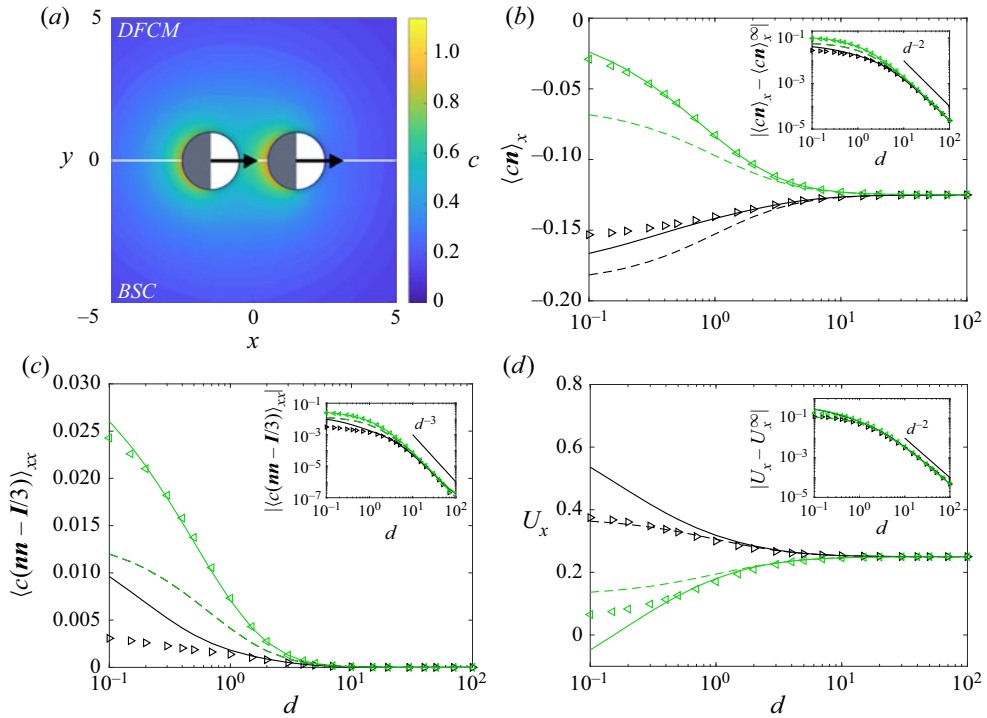


Figure 7. Case B. (a) Concentration field for $d = 1$ (upper half: DFCM, lower half: BSC), (b) first moment of concentration $\langle cn \rangle_x$, (c) second moment of concentration $\langle c(nn - I/3) \rangle_{xx}$, (d) velocity U_x . The black lines (and markers) correspond to particle 1 and the light green ones to particle 2. The triangle markers correspond to DFCM, the solid lines correspond to BSC, while the dashed lines to FFA. The inset shows the absolute values in logarithmic scale and the corresponding decay. The surface averages $\langle \dots \rangle$ were used for BSC and FFA, while the volume average $\{ \dots \}$ was used for DFCM. All the omitted components of $\langle cn \rangle$, $\langle c(nn - I/3) \rangle$ and U are zero.

studies (Varma & Michelin 2019; Nasouri & Golestanian 2020a). Furthermore, both particles point in the same direction so that, when far enough apart, they swim at the same velocity in the same direction.

Figure 7(a) shows the concentration field for $d = 1$: again, DFCM closely matches the BSC predictions. Here, both particles pump fluid from their front toward their active back cap where an excess solute concentration is produced, and therefore move along the $+e_x$ direction. As the interparticle distance shortens, the concentration increases in the gap, leading to enhanced (respectively decreased) surface gradients on the leading (respectively trailing) particle.

This physical intuition is confirmed by the evolution of the concentration polarity with the interparticle distance (figure 7b). The polarity matches that of an isolated particle $\langle cn \rangle^\infty = -\frac{1}{8}e_x$ for large distances $d \gg 1$, and is increased in magnitude for particle 1 (leader) while its magnitude decreases for particle 2 (follower) as d is reduced. The DFCM solution remains in close agreement with BSC for all distances (even down to a tenth of a radius), in particular capturing the asymmetric effect of the interaction on the two particles. In contrast, FFA predicts a symmetric progression of the polarity, leading to large discrepancies for $d < 3$. A similar behaviour is observed for the second moment (figure 7c), except for particle 1 for which it is underestimated by DFCM in the near field ($d < 1$). We note that although isolated Janus particles with uniform mobility behave as

neutral swimmers (exerting no force dipole or active stresslet on the fluid), their interaction leads to both of them acting as effective pushers on the fluid (negative stresslet, see (2.8)).

The velocity matches that of an isolated particle when $d \gg 1$, and the corrections introduced by the particles' interaction scale as $1/d^2$, as a result of the dominant phoretic repulsion (as for Case A); all three methods are able to capture this property (see figure 7(b,d), inset). Similarly, the second moment of surface concentration decreases as $1/d^3$ (figure 7c). As d is reduced, the combined effects of strong phoretic repulsion and hydrodynamic coupling (including the repulsion by the active stresslet) slow down and may even eventually reverse the swimming direction of particle 2 (figure 7d). Both our FCM solution and the FFA prediction show a qualitative agreement with the full solution (BSC) and predict the increase in velocity for the leading particle, while the trailing particle is slowed down. However, they fail to predict the reversal of the velocity of particle 2 observed in the full solution, although DFCM exhibits an appreciable improvement over FFA in the near field. A possible reason for this may be found in a dominant role of the lubrication layer separating the particles which is not well resolved in either approximation.

4.3. Janus particles – asymmetric configuration

Case B was still highly symmetric and further considered only uniform mobility, which is known to affect the hydrodynamic signature of the particle significantly (Lauga & Michelin 2016). In our third and final configuration, Case C (figure 5c), we consider a more generic interaction of two identical Janus particles with non-uniform mobility ($\alpha_n^F = 0$, $\alpha_n^B = 1$, $M_n^F = 0$, $M_n^B = 1$) positioned at an angle $\pi/4$ relative to the x -axis. Surface mobility results from the differential short-range interaction of solute and solvent molecules with the particle surface and, as such, is an intrinsic property of the particle's surface coating and may thus differ between the two caps of a Janus particle. For these particles, when isolated, the non-dimensional self-propulsion velocity is given by $U^\infty = \frac{1}{8}e_x$ (Golestanian *et al.* 2007). The convenient BSC approach is not usable in this non-axisymmetric setting, and although an extension to generic interactions of Janus particles is possible using full bispherical harmonics (Sharifi-Mood *et al.* 2016), it is sufficiently complex that direct numerical simulations using BEM proves in general more convenient, although the discontinuity of the mobility at the equator may introduce numerical errors, due to the singularity of the surface concentration gradient for a Janus particle (Michelin & Lauga 2014). In the following, we therefore compare our DFCM predictions to the solution obtained using BEM and the prediction of the far-field analysis (FFA).

The asymmetric concentration field obtained with DFCM in this configuration for $d = 1$ is shown on figure 8(a). Besides their intrinsic self-propulsion along $+e_x$ due to their self-generated surface chemical polarity, the accumulation of solute in the confined space between the particles introduces a phoretic repulsion along their line of centres (as for Case B), leading to an enhancement (respectively reduction) of both components of the velocity (U_x and U_y) for particle 1 (respectively particle 2). This behaviour is well captured by all three methods (figure 8b,c). Additionally, in the present configuration (Case C), the mobility is non-uniform: specifically here, we consider the case where the surface mobility of the front hemisphere is zero, so that only the back hemisphere generates a phoretic slip. As a result of the arrangement of the particles, the dominant slip along the surface of particle 1 (respectively particle 2) is therefore counter-clockwise (respectively clockwise) leading to a negative (respectively positive) rotation velocity Ω_z for that particle.

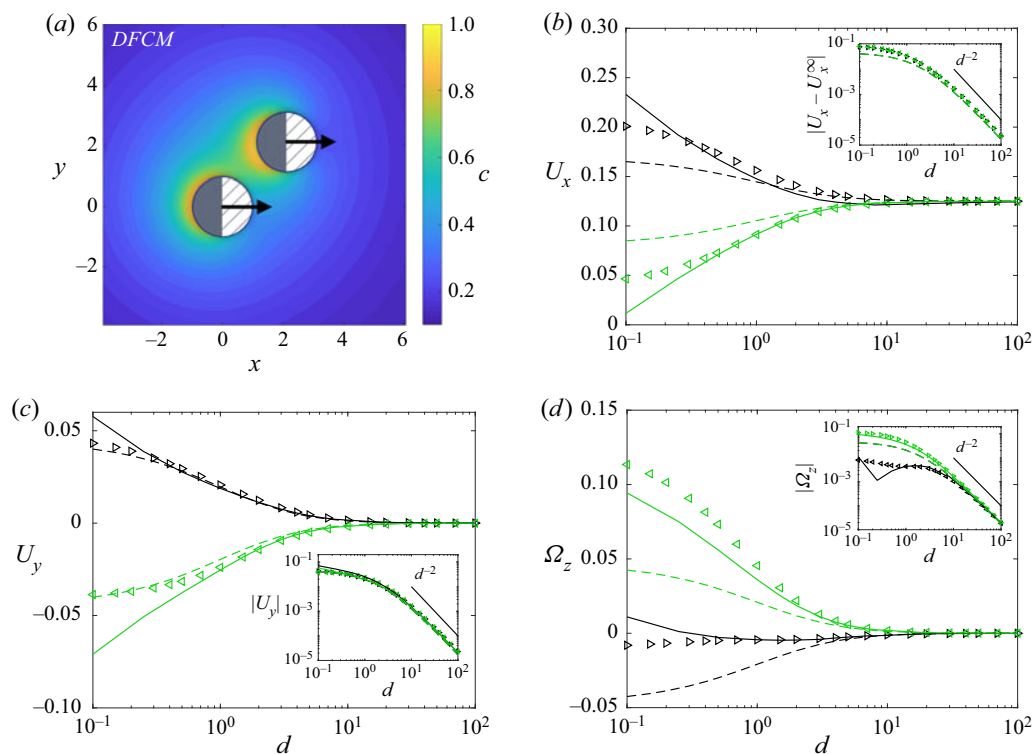


Figure 8. Case C. (a) DFCM concentration field for $d = 1$, (b) velocity U_x , (c) velocity U_y , (d) angular velocity Ω_z . The black lines (and markers) correspond to particle 1 and the light green ones to particle 2. The triangle markers correspond to DFCM, the solid lines correspond to BEM and the dashed lines to FFA. The inset shows the absolute values in logarithmic scale and the corresponding decay.

This rotation rate is proportional to the polarity, and therefore decays as $1/d^2$ in the far field. These intuitive trends are confirmed by the results of all three methods in figure 8(b–d).

As for Case B, when the interparticle distance d is reduced, these effects become more pronounced and the results obtained with DFCM for the translation velocity are in that regard slightly better than the predictions of FFA. However, FFA predicts a symmetric evolution of Ω_z with distance, while BEM, the most accurate solution, shows that particle 1 rotates slower than particle 2 for $d < 10$, and changes direction in the near field $d < 0.2$. DFCM is able to capture this non-trivial and asymmetric evolution of the rotation velocity, but fails to capture the direction reversal of particle 1; as for Case B, this may stem from the inability of DFCM to resolve correctly the lubrication flows within the thin fluid gap between the particles.

Nevertheless, over all three cases considered and in particular in the most generic setting of Janus particles with non-uniform mobility in non-axisymmetric settings, our results show the importance of the proper resolution of higher-order hydro-chemical multipolar signatures (e.g. induced polarities and rigidity stresslets) in order to capture accurately non-trivial features of the hydro-chemical interactions between particles. DFCM may not be able to resolve the details of the chemical and hydrodynamic fields in the gap between the surface of the particles when they are close to each other (e.g. $d \lesssim 0.5$) as it does not actually represent the exact position of the surface. Yet, this new numerical approach

offers significant improvements in capturing such complex effects both qualitatively and quantitatively in comparison with simpler analytical or numerical models, while providing a significant reduction in complexity in comparison with detailed numerical simulations such as BEM, opening significant opportunities for the numerical analysis of larger number of particles and suspension dynamics.

5. Discussion

In this work, we presented a generalization called DFCM of the approach of hydrodynamic FCM in order to compute hydro-chemical interactions within reactive suspensions of Janus particles with non-uniform surface activity and mobility. Following the standard hydrodynamic FCM, we rely on a truncated regularized multipolar expansion at the dipole level to solve the Laplace problem for the reactant concentration field, and its moments at the particle surface. While the monopole is directly obtained from the prescribed fluxes on the swimmer surface, the dipole is found iteratively by accounting for the effect of other particles on their polarity. Instead of using surface operators, which are difficult to handle on Eulerian grids, our method relies on spectrally convergent weighted volume averages to compute successive concentration moments. Unlike standard FCM, the averaging envelopes are non-Gaussian as their weight is shifted toward the particle's surface and thus differ from the Gaussian spreading envelopes associated with each singularity. The first two moments of concentration around the particle are directly related to the intrinsic phoretic velocity and rotation of the particles (i.e. those obtained for an isolated particle experiencing the same hydrodynamic surface slip in an unbounded domain) but also to the singularities characterizing their hydrodynamic signatures, i.e. an intrinsic active stresslet and a potential dipole. These multipoles are then used as inputs for the solution of the hydrodynamic (swimming) problem, solved using the existing hydrodynamic FCM framework to obtain the total particle velocities.

Even though our approximate method does not resolve the particle surface exactly (and is as such unable to capture lubrication or strong confinement effects), its predictions for the dynamics of two particles compare well with analytical or accurate numerical solutions for distances larger than half a radius ($d \gtrsim 0.5$), which is relevant for dilute and semi-dilute suspensions. Most importantly, in all the results presented above, DFCM provides significant improvements over far-field models that neglect mutually induced polarities and rigidity stresslets. Our case study has shown the importance of properly resolving these dipolar singularities to capture non-trivial hydro-chemical interactions between particles.

Although the present work purposely focuses on the presentation of the framework and detailed validation on pairwise interactions of phoretic particles, our diffusio-phoretic framework readily generalizes to N particles. A remarkable feature of FCM is that the spreading and averaging operations are volume based and independent of the Stokes and Laplace solvers. Instead of using Green's functions for specific geometries, the reactant concentration c and fluid velocity \mathbf{u} can be solved for with any numerical method (e.g. finite volume, spectral methods) on an arbitrary domain where the FCM spreading and averaging operations are performed on the fixed computational grid (Maxey & Patel 2001; Liu *et al.* 2009; Yeo & Maxey 2010). As shown in previous work (Delmotte *et al.* 2015), the corresponding cost scales linearly with the particle number $O(N)$, while Green's function-based methods, such as Stokesian dynamics (Brady & Bossis 1988) and the method of reflections (Varma & Michelin 2019), are restricted to simple geometries and require sophisticated techniques to achieve similar performances instead of their intrinsic quadratic scaling $O(N^2)$ (Liang *et al.* 2013; Fiore & Swan 2019; Yan & Blackwell 2020).

In addition to improving far-field models, our method therefore offers a scalable framework for large scale simulations of reactive particles. We will use these capacities to study their collective motion and characterize their macroscopic rheological response.

Despite its specific focus on the modelling of hydrochemical interactions within phoretic suspensions, the present analysis demonstrates how the fundamental idea of the original FCM can be extended and applied to other fields of physics. In such an approach the elliptic Stokes equations are solved over the entire domain (instead of the multiply connected fluid domain outside the particles) by introducing regularized forcings whose support is calibrated to account for the particle finite size and whose intensity is determined to account for a weak form of the boundary condition. For the chemical diffusion problem considered here, this amounts to (i) replacing a Laplace problem by a Poisson equation, (ii) calibrating the support of the spreading operators to match benchmark properties for a single particle and (iii) determining the forcing intensity by projecting the Neumann-type boundary condition on the particle surface onto a localized support function of appropriate shape (e.g. Gaussian or annular). This approach can readily be adapted for solving diffusion problems with more general (Dirichlet or mixed) boundary conditions, as encountered for more detailed chemical activity of reactive particles (Michelin & Lauga 2014; Tatulea-Codrean & Lauga 2018) or in bubble growth/dissolution problems (Michelin, Guérin & Lauga 2019), but also to other physical phenomena driven by elliptic equations, such as electromagnetic interactions of particles (Keaveny & Maxey 2008).

Funding. This work was supported by the European Research Council (ERC) under the European Union's Horizon 2020 research and innovation program (Grant Agreement No. 714027 to S.M.).

Declaration of interests. The authors report no conflict of interest.

Author ORCIDs.

Francisco Rojas-Pérez <https://orcid.org/0000-0002-9462-5671>;

Blaise Delmotte <https://orcid.org/0000-0002-9609-1175>;

Sébastien Michelin <https://orcid.org/0000-0002-9037-7498>.

Appendix A. Determining the source intensities

We consider here a single active particle bounded by a surface S . The concentration field outside S (in the fluid) satisfies Laplace's equation, and its value anywhere in the fluid domain can therefore be obtained in terms of its value and normal flux on S as

$$c(\mathbf{r}) = \frac{1}{4\pi} \int_S \left[c(\mathbf{s})\mathbf{n} \cdot \frac{(\mathbf{r} - \mathbf{s})}{|\mathbf{r} - \mathbf{s}|^3} + \left(-\frac{\partial c(\mathbf{s})}{\partial n} \right) \frac{1}{|\mathbf{r} - \mathbf{s}|} \right] dS, \tag{A1}$$

where $\mathbf{s} = a\mathbf{n}$ and \mathbf{r} are measured from the centre of the particle. Far from the particle (i.e. $|\mathbf{r}| \gg |s|$), and using the following Taylor expansion for $|\mathbf{r} - \mathbf{s}|^{-n}$,

$$\frac{1}{|\mathbf{r} - \mathbf{s}|^n} \approx \frac{1}{r^n} \left[1 + n \left(\frac{\mathbf{s} \cdot \mathbf{r}}{r^2} \right) + n \left(\frac{n}{2} + 1 \right) \left(\frac{\mathbf{s} \cdot \mathbf{r}}{r^2} \right)^2 + \dots \right], \tag{A2}$$

the concentration field can be expanded in terms of a series of singular multipoles, namely a monopole of intensity q^M , a dipole of intensity q^D (and up to the desired order of

approximation)

$$c(\mathbf{r}) = \frac{q^M}{4\pi r} + \frac{\mathbf{q}^D \cdot \mathbf{r}}{4\pi r^3} + \dots, \quad (\text{A3})$$

where the intensities are obtained as

$$q^M = \int_S \left(-\frac{\partial c(\mathbf{s})}{\partial n} \right) dS, \quad (\text{A4})$$

$$\mathbf{q}^D = a \int_S \left(-\frac{\partial c(\mathbf{s})}{\partial n} \mathbf{n} \right) dS + \int_S c(\mathbf{s}) \mathbf{n} dS. \quad (\text{A5})$$

Substitution of the boundary condition (2.1) leads to the result in (3.12a,b).

Appendix B. Intrinsic phoretic velocities and stresslet

The intrinsic phoretic velocity of a particle (i.e. its swimming speed in the absence of any hydrodynamic interactions or outer flow) is defined in (2.7a,b). Using the slip velocity definition in (2.3) and the mobility distribution as in (2.9), we obtain

$$\mathbf{U}_n^a = -\langle \mathbf{u}_s \rangle_n = -\bar{M}_n \langle \nabla_{\parallel} c \rangle_n - M_n^* \langle \text{sign}(\mathbf{p} \cdot \mathbf{n}) \nabla_{\parallel} c \rangle_n. \quad (\text{B1})$$

Integrating by parts the surface averaging operators we arrive at

$$\mathbf{U}_n^a = -\frac{2\bar{M}_n}{a} \langle c\mathbf{n} \rangle_n + \frac{M_n^* \mathbf{p}_n}{a} \langle c \rangle_n^{\text{eq}} - \frac{M_n^*}{a} (\langle c\mathbf{n} \rangle_n^+ - \langle c\mathbf{n} \rangle_n^-), \quad (\text{B2})$$

where the operators $\langle \dots \rangle_n^{\pm}$ refer to the mean value over the front and back caps of particle n , respectively, and $\langle \dots \rangle_n^{\text{eq}}$ is the line average over the equator of particle n . To compute these particular averages, we expand the surface concentration $c(\mathbf{n})$ in terms of its surface moments and truncate the expansion to the first three terms

$$c(\mathbf{n}) = \langle c \rangle_n + 3 \langle c\mathbf{n} \rangle_n \cdot \mathbf{n} + \frac{15}{2} \langle c(\mathbf{nn} - \mathbf{I}/3) \rangle_n : \mathbf{nn}. \quad (\text{B3})$$

Substitution in (B1) then finally provides

$$\mathbf{U}_n^a = -\frac{2\bar{M}_n}{a} \langle c\mathbf{n} \rangle_n - \frac{15M_n^*}{8a} \langle c(\mathbf{nn} - \mathbf{I}/3) \rangle_n : [\mathbf{p}_n \mathbf{I} + (\mathbf{p}_n \mathbf{I})^{\text{T}12} + \mathbf{p}_n \mathbf{p}_n \mathbf{p}_n], \quad (\text{B4})$$

which can be simplified into (3.46) using the symmetry and traceless property of $\mathbf{nn} - \mathbf{I}/3$.

Following a similar procedure, the intrinsic phoretic angular velocity can be expanded from (2.3), (2.7a,b) and (2.9) as

$$\boldsymbol{\Omega}_n^a = -\frac{3}{2a} \langle \mathbf{n} \times M \nabla_{\parallel} c \rangle_n = -\frac{3}{2a} \bar{M}_n \langle \mathbf{n} \times \nabla_{\parallel} c \rangle_n - \frac{3}{2a} M_n^* \langle \text{sign}(\mathbf{p} \cdot \mathbf{n}) \mathbf{n} \times \nabla_{\parallel} c \rangle_n, \quad (\text{B5})$$

and after integration by parts simplifies to

$$\boldsymbol{\Omega}_n^a = -\frac{3M_n^*}{2a^2} (\mathbf{p}_n \times \langle c\mathbf{n} \rangle_n^{\text{eq}}). \quad (\text{B6})$$

Substitution of (B3) provides the desired expression, (3.49).

The same method can also be applied to determine the intrinsic phoretic stresslet \mathbf{S}_n^a . From its definition in (2.8) and using (2.3) and (2.9), we obtain

$$\mathbf{S}_n^a = -10\pi a^2 \bar{M}_n \langle (\mathbf{n} \nabla_{\parallel} c + (\nabla_{\parallel} c) \mathbf{n}) \rangle_n - 10\pi a^2 M_n^* \langle \text{sign}(\mathbf{p} \cdot \mathbf{n}) (\mathbf{n} \nabla_{\parallel} c + (\nabla_{\parallel} c) \mathbf{n}) \rangle_n. \quad (\text{B7})$$

Integrating by parts the surface averaging operators provides

$$\begin{aligned} \mathbf{S}_n^a = & -60\pi a \bar{M}_n \langle c(\mathbf{nn} - \mathbf{I}/3) \rangle_n \\ & + 10\pi a M_n^* [\langle c \mathbf{n} \rangle_n^{eq} \mathbf{p}_n + \mathbf{p}_n \langle c \mathbf{n} \rangle_n^{eq} - 3 \langle (c(\mathbf{nn} - \mathbf{I}/3))_n^+ - (c(\mathbf{nn} - \mathbf{I}/3))_n^- \rangle]. \end{aligned} \quad (\text{B8})$$

Substitution of (B3) provides finally

$$\mathbf{S}_n^a = -60\pi a \bar{M}_n \langle c(\mathbf{nn} - \mathbf{I}/3) \rangle_n + \frac{15}{2} \pi a M_n^* [\langle (c \mathbf{n})_n \cdot \mathbf{p}_n \rangle (\mathbf{I} - \mathbf{p}_n \mathbf{p}_n) - \langle c \mathbf{n} \rangle_n \mathbf{p}_n - \mathbf{p}_n \langle c \mathbf{n} \rangle_n]. \quad (\text{B9})$$

REFERENCES

- ALARCÓN, F. & PAGONABARRAGA, I. 2013 Spontaneous aggregation and global polar ordering in squirmer suspensions. *J. Mol. Liq.* **185**, 56–61.
- ANDERSON, J.L. 1989 Colloid transport by interfacial forces. *Annu. Rev. Fluid Mech.* **21** (1), 61–99.
- BABATAHERI, A., ROPER, M., FERMIGIER, M. & DU ROURE, O. 2011 Tethered flexibmags as artificial cilia. *J. Fluid Mech.* **678**, 5–13.
- BATCHELOR, G.K. 1970 The stress system in a suspension of force-free particles. *J. Fluid Mech.* **41**, 545–570.
- BECHINGER, C., DI LEONARDO, R., LÖWEN, H., REICHHARDT, C., VOLPE, G. & VOLPE, G. 2016 Active particles in complex and crowded environments. *Rev. Mod. Phys.* **88**, 045006.
- BHALLA, A.P.S., GRIFFITH, B.E., PATANKAR, N.A. & DONEV, A. 2013 A minimally-resolved immersed boundary model for reaction-diffusion problems. *J. Chem. Phys.* **139** (21), 214112.
- BLAKE, J.R. 1971 A spherical envelope approach to ciliary propulsion. *J. Fluid Mech.* **46** (1), 199–208.
- BRADY, J.F. & BOSSIS, G. 1988 Stokesian dynamics. *Annu. Rev. Fluid Mech.* **20** (1), 111–157.
- BREGULLA, A.P. & CICHOS, F. 2015 Size dependent efficiency of photophoretic swimmers. *Faraday Discuss.* **184**, 381–391.
- BRENNEN, C. & WINET, H. 1977 Fluid mechanics of propulsion by cilia and flagella. *Annu. Rev. Fluid Mech.* **9**, 339–398.
- BROWN, A. & POON, W. 2014 Ionic effects in self-propelled pt-coated janus swimmers. *Soft Matt.* **10**, 4016–4027.
- BUTTINONI, I., VOLPE, G., KÜMMEL, F., VOLPE, G. & BECHINGER, C. 2012 Active Brownian motion tunable by light. *J. Phys.: Condens. Matter* **24**, 284129.
- CATES, M.E. & TAILLEUR, J. 2015 Motility-induced phase separation. *Annu. Rev. Condens. Ma. P.* **6**, 219–244.
- COLBERG, P.H. & KAPRAL, R. 2017 Many-body dynamics of chemically propelled nanomotors. *J. Chem. Phys.* **147** (6), 064910.
- CÓRDOVA-FIGUEROA, U.M. & BRADY, J.F. 2008 Osmotic propulsion: the osmotic motor. *Phys. Rev. Lett.* **100**, 158303.
- DANCE, S.L. & MAXEY, M.R. 2003 Incorporation of lubrication effects into the force-coupling method for particulate two-phase flow. *J. Comput. Phys.* **189** (1), 212–238.
- DELMOTTE, B., KEAVENY, E.E., PLOURABOUÉ, F. & CLIMENT, E. 2015 Large-scale simulation of steady and time-dependent active suspensions with the force-coupling method. *J. Comput. Phys.* **302**, 524–547.
- DREYFUS, R., BAUDRY, J., ROPER, M.L., FERMIGIER, M., STONE, H.A. & BIBETTE, J. 2005 Microscopic artificial swimmers. *Nature* **473**, 862–865.
- DUAN, W., WANG, W., DAS, S., YADAV, V., MALLOUK, T.E. & SEN, A. 2015 Synthetic nano- and micro-machines in analytical chemistry: sensing, migration, capture, delivery, and separation. *Annu. Rev. Anal. Chem.* **8**, 311–333.
- EBBENS, S.J. & HOWSE, J.R. 2010 In pursuit of propulsion at the nanoscale. *Soft Matt.* **6**, 726–738.
- ELGETI, J., WINKLER, R.G. & GOMPPER, G. 2015 Physics of microswimmers—single particle motion and collective behavior: a review. *Rep. Prog. Phys.* **78** (5), 056601.
- FAUCI, L. & DILLON, R. 2006 Biofluidmechanics of reproduction. *Annu. Rev. Fluid Mech.* **38**, 371–394.
- FIGLIORE, A.M. & SWAN, J.W. 2019 Fast Stokesian dynamics. *J. Fluid Mech.* **878**, 544–597.
- GINOT, F., THEURKAUFF, I., DETCHEVERRY, F., YBERT, C. & COTTIN-BIZONNE, C. 2018 Aggregation-fragmentation and individual dynamics of active clusters. *Nat. Commun.* **9**, 696.

Hydrochemical interactions of phoretic particles

- GOLESTANIAN, R., LIVERPOOL, T.B. & AJDARI, A. 2007 Designing phoretic micro- and nano-swimmers. *New J. Phys.* **9** (5), 126–126.
- GUASTO, J.S., RUSCONI, R. & STOCKER, R. 2012 Fluid mechanics of planktonic microorganisms. *Annu. Rev. Fluid Mech.* **44**, 373–400.
- HOWSE, J.R., JONES, R.A.L., RYAN, A.J., GOUGH, T., VAFABAKHSH, R. & GOLESTANIAN, R. 2007 Self-motile colloidal particles: from directed propulsion to random walk. *Phys. Rev. Lett.* **99**, 048102.
- HU, W.-F., LIN, T.-S., RAFAI, S. & MISBAH, C. 2019 Chaotic swimming of phoretic particles. *Phys. Rev. Lett.* **123** (23), 238004.
- IBRAHIM, Y., GOLESTANIAN, R. & LIVERPOOL, T.B. 2017 Multiple phoretic mechanisms in the self-propulsion of a pt-insulator janus swimmer. *J. Fluid Mech.* **828**, 318–352.
- IBRAHIM, Y. & LIVERPOOL, T.B. 2016 How walls affect the dynamics of self-phoretic microswimmers. *Eur. Phys. J.* **225**, 1843–1874.
- ISHIKAWA, T., SIMMONDS, M.P. & PEDLEY, T.J. 2006 Hydrodynamic interaction of two swimming model micro-organisms. *J. Fluid Mech.* **568**, 119–160.
- IZRI, Z., VAN DER LINDEN, M.N., MICHELIN, S. & DAUCHOT, O. 2014 Self-propulsion of pure water droplets by spontaneous marangoni-stress-driven motion. *Phys. Rev. Lett.* **113**, 248302.
- KAGAN, D., LAOCHAROENSUK, R., ZIMMERMAN, M., CLAWSON, C., BALASUBRAMANIAN, S., KANG, D., BISHOP, D., SATTAYASAMITHIT, S., ZHANG, L. & WANG, J. 2010 Rapid delivery of drug carriers propelled and navigated by catalytic nanoshuttles. *Small* **6** (23), 2741–2747.
- KANSO, E. & MICHELIN, S. 2019 Phoretic and hydrodynamic interactions of weakly confined autophoretic particles. *J. Chem. Phys.* **150**, 044902.
- KEAVENY, E.E. & MAXEY, M.R. 2008 Modeling the magnetic interactions between paramagnetic beads in magnetorheological fluids. *J. Comput. Phys.* **227**, 9554–9571.
- KÜMMEL, F., TEN HAGEN, B., WITTKOWSKI, R., BUTTINONI, I., EICHHORN, R., VOLPE, G., LÖWEN, H. & BECHINGER, C. 2013 Circular motion of asymmetric self-propelling particles. *Phys. Rev. Lett.* **110**, 198302.
- LADD, A.J.C. & VERBERG, R. 2001 Lattice-Boltzmann simulations of particle-fluid suspensions. *J. Stat. Phys.* **104** (5), 1191–1251.
- LAMBERT, R.A., PICANO, F., BREUGEM, W.P. & BRANDT, L. 2013 Active suspensions in thin films: nutrient uptake and swimmer motion. *J. Fluid Mech.* **733**, 528–557.
- LAUGA, E. 2016 Bacterial hydrodynamics. *Annu. Rev. Fluid Mech.* **48**, 105–130.
- LAUGA, E. & MICHELIN, S. 2016 Stresslets induced by active swimmers. *Phys. Rev. Lett.* **117**, 148001.
- LAUGA, E. & POWERS, T.R. 2009 The hydrodynamics of swimming microorganisms. *Rep. Prog. Phys.* **72** (9), 096601.
- LI, J., SHKLYAEV, O.E., LI, T., LIU, W., SHUM, H., ROZEN, I., BALAZS, A.C. & WANG, J. 2015 Self-propelled nanomotors autonomously seek and repair cracks. *Nano Lett.* **15** (10), 7077–7085.
- LIANG, Z., GIMBUTAS, Z., GREENGARD, L., HUANG, J. & JIANG, S. 2013 A fast multipole method for the Rotne-Prager-Yamakawa tensor and its applications. *J. Comput. Phys.* **234**, 133–139.
- LIEBCHEN, B. & LÖWEN, H. 2019 Which interactions dominate in active colloids? *J. Chem. Phys.* **150**, 061102.
- LIEBCHEN, B., MARENDUZZO, D., PAGONABARRAGA, I. & CATES, M.E. 2015 Clustering and pattern formation in chemorepulsive active colloids. *Phys. Rev. Lett.* **115**, 258301.
- LIU, D., KEAVENY, E.E., MAXEY, M.R. & KARNIADAKIS, G.E. 2009 Force-coupling method for flows with ellipsoidal particles. *J. Comput. Phys.* **228** (10), 3559–3581.
- LOMHOLT, S. & MAXEY, M.R. 2003 Force-coupling method for particulate two-phase flow: Stokes flow. *J. Comput. Phys.* **184** (2), 381–405.
- LUSHI, E. & PESKIN, C.S. 2013 Modeling and simulation of active suspensions containing large numbers of interacting micro-swimmers. *Comput. Struct.* **122**, 239–248.
- MAASS, C.C., KRÜGER, C., HERMINGHAUS, S. & BAHR, C. 2016 Swimming droplets. *Annu. Rev. Condens. Ma. P.* **7**, 171–193.
- MARCHETTI, M.C., JOANNY, J.F., RAMASWAMY, S., LIVERPOOL, T.B., PROST, J., RAO, M. & SIMHA, R.A. 2013 Hydrodynamics of soft active matter. *Rev. Mod. Phys.* **85**, 1143–1189.
- MAXEY, M. & PATEL, B.K. 2001 Localized force representations for particles sedimenting in stokes flow. *Intl J. Multiphase Flow* **27**, 1603–1626.
- MICHELIN, S., GUÉRIN, E. & LAUGA, E. 2019 Collective dissolution of microbubbles. *Phys. Rev. Fluids* **3**, 043601.
- MICHELIN, S. & LAUGA, E. 2014 Phoretic self-propulsion at finite Péclet numbers. *J. Fluid Mech.* **747**, 572–604.
- MICHELIN, S. & LAUGA, E. 2015 Autophoretic locomotion from geometric asymmetry. *Eur. Phys. J. E* **38**, 7.

- MICHELIN, S., LAUGA, E. & BARTOLO, D. 2013 Spontaneous autophoretic motion of isotropic particles. *Phys. Fluids* **25** (6), 061701.
- MONTENEGRO-JOHNSON, T.D., MICHELIN, S. & LAUGA, E. 2015 A regularised singularity approach to phoretic problems. *Eur. Phys. J. E* **38** (12), 139.
- MORAN, J.L. & POSNER, J.D. 2011 Electrokinetic locomotion due to reaction-induced charge auto-electrophoresis. *J. Fluid Mech.* **680**, 31–66.
- MORAN, J.L. & POSNER, J.D. 2017 Phoretic self-propulsion. *Annu. Rev. Fluid Mech.* **49**, 511–540.
- NASOURI, B. & GOLESTANIAN, R. 2020a Exact axisymmetric interaction of phoretically active janus particles. *J. Fluid Mech.* **905**, A13.
- NASOURI, B. & GOLESTANIAN, R. 2020b Exact phoretic interaction of two chemically active particles. *Phys. Rev. Lett.* **124**, 168003.
- PAK, O.S. & LAUGA, E. 2014 Generalized squirming motion of a sphere. *J. Engng Maths* **88**, 1–28.
- PAXTON, W.F., KISTLER, K.C., OLMEDA, C.C., SEN, A., ANGELO, S.K.S., CAO, Y., MALLOW, T.E., LAMMERT, P.E. & CRESPI, V.H. 2004 Catalytic nanomotors: autonomous movement of striped nanorods. *J. Am. Chem. Soc.* **126** (41), 13424–1343.
- PEDLEY, T.J. & KESSLER, J.O. 1992 Hydrodynamics phenomena in suspensions of swimming microorganisms. *Annu. Rev. Fluid Mech.* **24**, 313–358.
- PERRO, A., RECLUS, S., RAVAIN, S., BOURGEAT-LAMI, E. & DUGUET, E. 2005 Design and synthesis of janus micro- and nanoparticles. *J. Mater. Chem.* **15**, 3745–3760.
- POPESCU, M.N., USPAL, W.E. & DIETRICH, S. 2016 Self-diffusiophoresis of chemically active colloids. *Eur. Phys. J.* **225**, 2189–2206.
- REIGH, S.Y. & KAPRAL, R. 2015 Catalytic dimer nanomotors: continuum theory and microscopic dynamics. *Soft Matt.* **11**, 3149–3158.
- SAFFMAN, P.G. 1973 On the settling speed of free and fixed suspensions. *Stud. Appl. Maths* **52** (2), 115–127.
- SAHA, S., GOLESTANIAN, R. & RAMASWAMY, S. 2014 Clusters, asters, and collective oscillations in chemotactic colloids. *Phys. Rev. E* **89**, 062316.
- SAINTILLAN, D. 2018 Rheology of active fluids. *Annu. Rev. Fluid Mech.* **50**, 563–592.
- SAINTILLAN, D. & SHELLEY, M.J. 2013 Active suspensions and their nonlinear models. *C. R. Phys.* **14** (6), 497–517.
- SCHMIDT, F., LIEBCHEN, B., LÖWEN, H. & VOLPE, G. 2019 Light-controlled assembly of active colloidal molecules. *J. Chem. Phys.* **150** (9), 094905.
- SHAO, J., ABDELGHANI, M., SHEN, G., CAO, S., WILLIAMS, D.S. & VAN HEST, J.C.M. 2018 Erythrocyte membrane modified janus polymeric motors for thrombus therapy. *ACS Nano* **12** (5), 4877–4885.
- SHARIFI-MOOD, N., MOZZAFARI, A. & CORDOVA-FIGUEROA, U.M. 2016 Pair interaction of catalytically active colloids: from assembly to escape. *J. Fluid Mech.* **798**, 910–954.
- SHKLYAEV, S., BRADY, J.F. & CORDOVA-FIGUEROA, U.M. 2014 Non-spherical osmotic motor: chemical sailing. *J. Fluid Mech.* **748**, 488–520.
- SIEROU, A. & BRADY, J.F. 2001 Accelerated Stokesian dynamics simulations. *J. Fluid Mech.* **448**, 115–146.
- SINGH, R. & ADHIKARI, R. 2019 Pystokes: Phoresis and Stokesian hydrodynamics in python. [arXiv:1910.00909](https://arxiv.org/abs/1910.00909).
- SINGH, R., ADHIKARI, R. & CATES, M.E. 2019 Competing chemical and hydrodynamic interactions in autophoretic colloidal suspensions. *J. Chem. Phys.* **151** (4), 044901.
- SOTO, R. & GOLESTANIAN, R. 2014 Self-assembly of catalytically active colloidal molecules: tailoring activity through surface chemistry. *Phys. Rev. Lett.* **112**, 068301.
- SOTO, R. & GOLESTANIAN, R. 2015 Self-assembly of active colloidal molecules with dynamic function. *Phys. Rev. E* **91**, 052304.
- STONE, H.A. & SAMUEL, A.D.T. 1996 Propulsion of microorganisms by surface distortions. *Phys. Rev. Lett.* **77**, 4102.
- SUNDARARAJAN, S., LAMMERT, P.E., ZUDANS, A.W., CRESPI, V.H. & SEN, A. 2008 Catalytic motors for transport of colloidal cargo. *Nano Lett.* **8** (5), 1271–1276.
- SWAN, J.W., BRADY, J.F. & MOORE, R.S. 2011 Modeling hydrodynamic self-propulsion with Stokesian dynamics. Or teaching Stokesian dynamics to swim. *Phys. Fluids* **23** (7), 071901.
- TATULEA-CODREAN, M. & LAUGA, E. 2018 Artificial chemotaxis of phoretic swimmers: instantaneous and long-time behaviour. *J. Fluid Mech.* **856**, 921–957.
- THEURKAUFF, I., COTTIN-BIZONNE, C., PALACCI, J., YBERT, C. & BOCQUET, L. 2012 Dynamic clustering in active colloidal suspensions with chemical signaling. *Phys. Rev. Lett.* **108**, 268303.
- THUTUPALLI, S., GEYER, D., SINGH, R., ADHIKARI, R. & STONE, H.A. 2018 Flow-induced phase separation of active particles is controlled by boundary conditions. *Proc. Natl Acad. Sci. USA* **115**, 5403–5408.

Hydrochemical interactions of phoretic particles

- TRAVERSO, T. & MICHELIN, S. 2020 Hydrochemical interactions in dilute phoretic suspensions: from individual particle properties to collective organization. *Phys. Rev. Fluids* **5**, 104203.
- USPAL, W.E., POPESCU, M.N., DIETRICH, S. & TASINKEVYCH, M. 2015 Self-propulsion of a catalytically active particle near a planar wall: from reflection to sliding and hovering. *Soft Matt.* **11**, 434–438.
- VARMA, A. & MICHELIN, S. 2019 Modeling chemo-hydrodynamic interactions of phoretic particles: a unified framework. *Phys. Rev. Fluids* **4**, 124204.
- VARMA, A., MONTENEGRO-JOHNSON, T.D. & MICHELIN, S. 2018 Clustering-induced self-propulsion of isotropic autophoretic particles. *Soft Matt.* **14**, 7155–7173.
- WANG, Y., HERNANDEZ, R.M. JR., BARTLETT, D.J., BINGHAM, J.M., KLINE, T.R., SEN, A. & MALLOUK, T.E. 2006 Bipolar electrochemical mechanism for the propulsion of catalytic nanomotors in hydrogen peroxide solutions. *Langmuir* **22**, 10451–10456.
- XU, J., MAXEY, M.R. & KARNIADAKIS, G.E.M. 2002 Numerical simulation of turbulent drag reduction using micro-bubbles. *J. Fluid Mech.* **468**, 271–281.
- YADAV, V., DUAN, W., BUTLER, P.J. & SEN, A. 2015 Anatomy of nanoscale propulsion. *Annu. Rev. Biophys.* **44**, 77–100.
- YAN, W. & BLACKWELL, R. 2020 Kernel aggregated fast multipole method: efficient summation of Laplace and Stokes kernel functions. [arXiv:2010.15155](https://arxiv.org/abs/2010.15155).
- YAN, W. & BRADY, J.F. 2016 The behavior of active diffusiophoretic suspensions: an accelerated Laplacian dynamics study. *J. Chem. Phys.* **145** (13), 134902.
- YANG, M., WYSOCKI, A. & RIPOLL, M. 2014 Hydrodynamic simulations of self-phoretic microswimmers. *Soft Matt.* **10**, 6208–6218.
- YARIV, E. 2011 Electrokinetic self-propulsion by inhomogeneous surface kinetics. *Proc. R. Soc. Lond. A* **467**, 1645–1664.
- YEO, K. & MAXEY, M.R. 2010 Simulations of concentrated suspensions using the force-coupling method. *J. Comput. Phys.* **229**, 2401–2421.
- YI, Y., SANCHEZ, L., GAO, Y. & YU, Y. 2016 Janus particles for biological imaging and sensing. *Analyst* **141** (12), 3526–3539.
- ZHANG, L., ABBOTT, J.J., DONG, L., KRATOCHVIL, B.E., BELL, D. & NELSON, B.J. 2009 Artificial bacterial flagella: fabrication and magnetic control. *Appl. Phys. Lett.* **94**, 064107.
- ZÖTTL, A. & STARK, H. 2014 Hydrodynamics determines collective motion and phase behavior of active colloids in quasi-two-dimensional confinement. *Phys. Rev. Lett.* **112**, 118101.
- ZÖTTL, A. & STARK, H. 2016 Emergent behavior in active colloids. *J. Phys.: Condens. Matter* **28** (25), 253001.
- ZÖTTL, A. & STARK, H. 2018 Simulating squirmers with multiparticle collision dynamics. *Eur. Phys. J. E* **41** (5), 61.